

# Instantaneous physics-based ground motion maps using reduced-order modeling

John M. Rekoske<sup>1</sup>, Alice-Agnes Gabriel<sup>1,2</sup>, Dave A. May<sup>1</sup>

<sup>1</sup>Scripps Institution of Oceanography, University of California San Diego, La Jolla, USA

<sup>2</sup>Department of Earth and Environmental Sciences, Ludwig-Maximilians-Universität München, Munich, Germany

## Key Points:

- Physics-based simulations are useful for seismic hazard assessment and ground motion prediction but are computationally expensive.
- Our reduced-order model accurately predicts simulated peak ground velocities for scenarios, including 3D wavefield and topographic effects.
- The reduced-order model produces physics-based ground motion maps in milliseconds for variable source depths and focal mechanisms.

arXiv:2212.11335v2 [physics.geo-ph] 26 Jul 2023

---

Corresponding author: John M. Rekoske, [jrekoske@ucsd.edu](mailto:jrekoske@ucsd.edu)

**Abstract**

Physics-based simulations of earthquake ground motion are useful to complement recorded ground motions. However, the computational expense of performing numerical simulations hinders their applicability to tasks that require real-time solutions or ensembles of solutions for different earthquake sources. To enable rapid physics-based solutions, we present a reduced-order modeling (ROM) approach based on interpolated proper orthogonal decomposition (POD) to predict peak ground velocities (PGVs). As a demonstrator, we consider PGVs from regional 3D wave propagation simulations at the location of the 2008 Mw 5.4 Chino Hills earthquake using double-couple sources with varying depth and focal mechanisms. These simulations resolve frequencies  $\leq 1.0$  Hz and include topography, viscoelastic attenuation, and S-wave speeds  $\geq 500$  m/s. We evaluate the accuracy of the interpolated POD ROM as a function of the approximation method. Comparing the radial basis function (RBF), multilayer perceptron neural network, random forest, and  $k$ -nearest neighbor, we find that the RBF interpolation gives the lowest error ( $\approx 0.1$  cm/s) when tested against an independent dataset. We also find that evaluating the ROM is  $10^7 - 10^8$  times faster than the wave propagation simulations. We use the ROM to generate PGV maps for one million different focal mechanisms, in which we identify potentially damaging ground motions and quantify correlations between focal mechanism, depth, and accuracy of the predicted PGV. Our results demonstrate that the ROM can rapidly and accurately approximate the PGV from wave propagation simulations with variable source properties, topography, and complex subsurface structure.

**Plain Language Summary**

Computer simulations can be used to predict the intensity of ground shaking caused by earthquakes. However, these simulations require significant amounts of computing time to obtain accurate results, making them too slow for real-time systems. In this work, we apply a technique that allows us to obtain instantaneous and accurate approximations of a scenario earthquake simulation using simplified models. The simplified models are fast enough to evaluate this earthquake scenario on demand. We use the simplified models to predict shaking intensities for one million different fault planes at the location of the 2008 Chino Hills earthquake. By analyzing the predicted shaking intensities from these earthquakes, we identify possible areas of strong shaking, areas that might otherwise be unidentified if fewer earthquake scenarios were examined. These results suggest that these types of simplified models could be considered to assess regional earthquake hazards and to inform shaking intensity predictions in earthquake early warning.

**1 Introduction**

A fundamental challenge in seismology and earthquake engineering is the estimation of the ground shaking caused by earthquakes, especially for areas with high population densities or containing critical infrastructure and in the near-source region where observations are sparse. For example, after large earthquakes, it is important to rapidly characterize the shaking intensity to identify areas of potential damage and guide rapid response efforts. Accurately estimating shaking intensities in near-real-time is one of the

primary goals of the ShakeMap product developed by the U.S. Geological Survey (Worden & Wald, 2016). Additionally, real-time estimates of the expected ground motion intensity are needed in earthquake early warning (EEW) to issue alerts to people and critical systems, ideally in advance of the strongest shaking (Kohler et al., 2017). Also, systematically quantifying the potential level of ground shaking from as of yet unobserved earthquakes that may someday occur is important for earthquake preparedness and seismic hazard assessment (e.g., Graves et al., 2011; Baker et al., 2014; Bommer et al., 2010).

Several strategies have been developed to estimate earthquake ground motions. Instrumental recordings and non-instrumental data such as “Did You Feel It?” reports (Wald et al., 2011) directly inform the amplitudes and spatial distribution of seismic ground motion. However, the generally sparse spatial coverage of observations leads to significant uncertainties in the shaking distributions (Wald et al., 2008). To fill in the gaps, recent approaches include spatial and spectral interpolation (Worden et al., 2018), Gaussian process regression (Tamhidi et al., 2021), and conditional simulation (Engler et al., 2022; Bailey et al., 2022), but rapidly estimating the full distribution of shaking intensity remains a challenge. Most EEW systems and large-scale seismic hazard studies (e.g., Stirling et al., 2012; Kohler et al., 2017; Petersen et al., 2020; Meletti et al., 2021) instead use empirical ground motion models (GMMs) which give instantaneous ground motion estimates for given source, path, and site parameters. GMMs rely on the availability of a large ground motion dataset recorded in a specific region or tectonic setting (e.g., Bozorgnia et al., 2014, 2021; Goulet et al., 2021), which may not always be available. Thus, GMMs typically rely on the ergodic assumption (Anderson & Brune, 1999) where all the data from a certain tectonic environment are grouped together to develop a single model that describes the average scaling with magnitude, distance, and site conditions. However, the uncertainty of GMM predictions can be reduced with nonergodic source, path, or site correction terms if they are well-constrained (e.g., Baltay et al., 2017; Sahakian et al., 2019; Parker & Baltay, 2022). Going beyond the source-based approach of GMMs, other methods have been developed that directly use ground motion or wavefield observations to forecast the shaking at distant locations (Hoshiaba & Aoki, 2015; Kodera et al., 2018; Furumura et al., 2019; Cochran et al., 2019; Oba et al., 2020). A recent wavefield-based approach developed by Nagata et al. (2023) uses reduced-order modeling to reconstruct seismic wavefields from sparse measurements, although their approach does not include the source parameterization that is needed to solve inverse problems.

Complementary to GMM and wavefield-based prediction techniques, numerical simulations of earthquake rupture and seismic wave propagation provide physics-informed estimates of shaking intensity (e.g., Aagaard et al., 2001; K. B. Olsen et al., 2006; Moschetti et al., 2017; Rodgers et al., 2020; Taufiqurrahman et al., 2022). These simulations can assume a kinematic description of the earthquake source (e.g., Graves & Pitarka, 2016), or solve for the earthquake slip history with spontaneous dynamic rupture models (e.g., Ripperger et al., 2008; Withers et al., 2018). In both cases, the seismic wave equation is solved to simulate the propagation of seismic waves within the Earth. Physics-based 3D ground motion simulations have advanced in terms of realism and agreement with real data due to increasingly dense observations, a better understanding of Earth struc-

ture and ever-increasing computing power. For example, recent advances in community velocity model (CVM) development in southern California have been used to inform physics-based seismic hazard assessment (Graves et al., 2011; Milner et al., 2021). Important progress has been made in generating broadband synthetics which usually involve a stochastic component for the high frequencies (e.g., Boore, 1983; A. Frankel et al., 2018).

Deterministically resolving the high-frequency wavefield makes physics-based ground motion modeling computationally expensive, typically requiring high-performance computing (HPC) technology (e.g., Cui et al., 2013; Heinecke et al., 2014; Rodgers et al., 2020; Savran & Olsen, 2020; Pitarka et al., 2022). The high cost of each high-resolution numerical simulation challenges applications in which many forward models must be evaluated, such as dynamic earthquake source inversion problems (e.g., Gallovič et al., 2019) or physics-based probabilistic seismic hazard assessment. Even though modeling simplifications help reduce the computational expense (e.g., by setting an upper threshold for the minimum S-wave velocity,  $V_S$ ), regional-scale broadband simulations can require up to  $10^3$ – $10^4$  CPU hours (CPUh) of computing time (e.g., Hu et al., 2022; Taufiqurrahman et al., 2022).

To address these challenges, recent efforts have enabled the rapid generation of synthetic seismograms using Green’s functions or deep learning. For global seismology, 1.0 Hz discrete Green’s functions for axisymmetric Earth models are available on-demand via InstaSeis (van Driel et al., 2015), and 3D Green’s functions based on the spectral element method (Komatitsch & Tromp, 1999) are typically available a few hours after  $M_w > 5.5$  earthquakes (Tromp et al., 2010). However, the limited resolution of global approaches are not suitable for regional ground motion applications. At the regional scale, Wang and Zhan (2020) created a 0.5 Hz 3D Green’s function database for stations in the southern California seismic network to enable real-time moment tensor inversions with 3D models. However, such Green’s function databases often require several terabytes of storage, presenting a major challenge in accessibility. Other approaches used deep learning to learn approximate solutions to the wave equation and produce seismograms for arbitrary velocity models (Moseley et al., 2018, 2020; Smith et al., 2020; Yang et al., 2021, 2023; Rasht-Behesht et al., 2022) or create neural network GMMs based on simulations (Withers et al., 2020). However, machine-learning approaches have not yet directly reproduced 3D path or topographic effects that are important for ground motion prediction.

Here, we present a surrogate modeling approach that aims to address the need for rapid generation of 3D physics-based synthetics and ground motion intensity maps. Our approach is based on a reduced-order model (ROM), a particular type of surrogate model. In the model order reduction framework, a high-fidelity forward model can be approximated by a surrogate model, which typically has many fewer degrees of freedom and is fast to evaluate. As a result, a well-trained ROM can enable real-time and many-query evaluation of a system and can closely approximate the solution of an expensive forward simulation. We predict the peak-ground velocity (PGV) from a scenario of regional ground motion simulation. Our method produces physics-informed estimates instantaneously, thus, at the same speed as GMMs. While ROMs have rarely been applied in geophysics thus far, they have been demonstrated to accurately approximate solutions to linear and

non-linear physics-based models in other fields of science and engineering (e.g., Willcox & Peraire, 2002; Benner et al., 2015; Hesthaven et al., 2022).

The structure of this paper is organized as follows. We first provide an overview of our ROM development workflow based on an interpolated proper orthogonal decomposition (iPOD) technique in Section 2.1. We use simulations to create simulated PGV maps for different earthquake sources and decompose them using iPOD. We create the ROM by fitting function approximators that predict the iPOD coefficients for different values of the input source parameters. We can then use the ROM to instantaneously predict PGV maps for new earthquakes that were not modeled. We describe the details of the forward problems for both a 1D layered and a 3D velocity model with topography in Section 2.2. We describe how we will use four different function approximators to predict the simulation output in Section 2.3. In our results Section 3, we evaluate the accuracy of the ROMs using an independent testing dataset. We provide illustrative examples highlighting the ROM’s ability to reproduce PGV maps faithfully. Finally, we present a potential application and sensitivity analysis emphasizing the importance of hypocentral depth in PGV predictions. Lastly, we discuss in Section 4 how reduced-order modeling may path new avenues for physics-based hazard analysis and for using high-performance computing empowered simulations in real-time systems by enabling the instantaneous generation of physics-informed ground motion maps.

## 2 Methods

### 2.1 Reduced-order modeling workflow

We consider the earthquake source to be a point source in space, parameterized by its hypocentral depth, strike, dip, and rake. These four parameters will be denoted by  $\mathbf{p}$ . The ground motion intensity metric we use is the surface peak-ground velocity (PGV) denoted by  $\mathbf{q}$ . We define the mapping between the parameters  $\mathbf{p}$  and the PGV  $\mathbf{q}$  using a physics-based approach given by the (visco-)elastic wave equation for an isotropic medium. When a 3D velocity model is used to describe the Earth’s crustal structure and/or non-planar topography is considered, this problem must be solved numerically. The computational cost of performing these numerical wave propagation simulations precludes their direct usage within real-time or rapid response infrastructure, as well as many-query tasks, for example as required for global sensitivity analysis and forward uncertainty quantification.

Referring to the numerical method used to solve the wave equation and produce the PGV  $\mathbf{q}$  as the full-order model (FOM), we wish to construct a reduced-order model (ROM) that approximates  $\mathbf{q}$  given the earthquake parameters  $\mathbf{p}$  as input (Figure 1). While solving the FOM is a computationally expensive problem that requires HPC, the ROM has fewer degrees of freedom resulting in lower computational complexity compared to the FOM. Thus, the ROM is much faster to evaluate than the FOM. To inform the ROM, we obtain FOM solutions for a set of points  $\{\mathbf{p}_1, \mathbf{p}_2, \dots, \mathbf{p}_{n_s}\}$  where  $n_s$  is the total number of simulations that will be performed. Each parameter vector  $\mathbf{p}_i$  is contained within the four-dimensional space  $\mathcal{P}$  which encompasses the range of source depths and focal

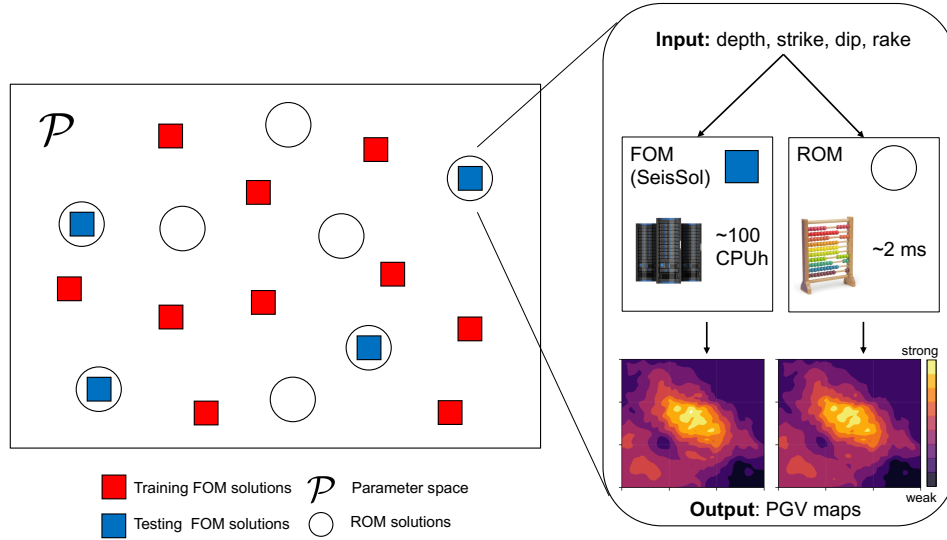


Figure 1: Conceptual illustration of the reduced-order model (ROM) development and validation procedures. We first obtain full-order model (FOM) solutions for points in the parameter space  $\mathcal{P}$  and divide them into training (red squares) and testing solutions (blue squares). Here, FOM refers to the forward problem of a numerical solution of the wave equation and producing a surface peak ground velocity (PGV) map. After training the ROM using the training FOM solutions, one can evaluate the ROM for any new point in  $\mathcal{P}$  (open circles). The ROM solutions are validated against the testing FOM solutions (overlapping circles and blue squares). As shown on the right, the FOM and ROM output similar PGV maps that depend on the input source parameters; the ROM, however, is a computationally inexpensive model with fewer degrees of freedom.

mechanism angles we consider; the ROM is only applicable for sources contained within  $\mathcal{P}$ . We then split the set of FOM solutions into two groups: training FOM solutions and testing FOM solutions. After using the training FOM solutions to train the ROM, we validate it against the testing FOM solutions. If there is a good agreement, then the ROM can be used as an efficient substitute, or surrogate, for the FOM.

## 2.2 Forward model

Our forward problem is the simulation of PGV maps that result from earthquakes with a given hypocentral depth and focal mechanism. We numerically simulate the 3D propagation of seismic waves produced by each source, varying the strike, dip, rake, and hypocentral depth of the source in each simulation. Our source parameterization is motivated by seismicity in Southern California (SCEDC, 2013; Field et al., 2014) but simplified for the proof-of-concept scope of this study. As a source-time function that describes the rate of earthquake moment release, we use  $\dot{M}(t) = \frac{M_0 t}{T^2} e^{-t/T}$  with  $T = 0.4$  s. This results in a Brune-type source spectrum with a stress drop of approximately 5.0

MPa (Brune, 1970). We do not vary the total scalar seismic moment, prescribing  $M_w = 5.4$  in all simulations. We assume point-source, double-couple moment tensor earthquake source descriptions, which is a reasonable assumption for most small earthquakes resulting from shear faulting (Julian et al., 1998). The hypocentral depths vary from 2.0 to 20.0 km.

To generate ground motion maps from the seismic wave simulations for each source, we first define a high-resolution area of interest. We select a 30 km by 30 km square area (Figure 2a) centered at the epicenter of the 2008  $M_w$  5.4 Chino Hills earthquake (33.949° N, 117.776° W), an area that has potentially significant topographic and basin effects on ground motion (Taborda & Bielak, 2013). Note that the complete computational mesh is larger (150 × 150 × 100 km) than the area of interest to prevent artificial boundary reflections from affecting the PGV measurements. We limit the computational expense of the forward simulations by selecting  $f_{max} = 1.0$  Hz as the maximum frequency to fully resolve.

For each earthquake source, we perform forward simulations with three different setups of increasing complexity (Figure 2b). The first setup uses a flat, layer-over-halfspace velocity model, which defines a 1D velocity structure (denoted as “LOH”, see Table S1 for the material parameters). The second setup “3D-1400” uses a 3D community velocity model for Southern California, SCEC CVM-H v15.1.0 (Shaw et al., 2015), and includes topography. “1400” indicates that we set a floor for the minimum S-wave velocity at  $V_{S,min} = 1400$  m/s. In both LOH and 3D-1400, we assume linear, elastic wave propagation. The third setup “3D-500A” is similar to 3D-1400 except that  $V_{S,min} = 500$  m/s and that we account for frequency-independent viscoelastic attenuation with  $Q_p = 0.1V_S$  and  $Q_s = 0.05V_S$  (for  $V_S$  measured in m/s) (K. Olsen et al., 2003). The viscoelastic attenuation setup assumes a Maxwell material with three damping mechanisms with their respective relaxation frequencies of 0.05, 0.5, and 5.0 Hz (Uphoff et al., 2017a). These different modeling setups allow us to examine how the ROM predictions and accuracies are affected by the modeling assumptions related to each simulation regime.

To perform the seismic wave propagation simulations for each source, we use SeisSol (<https://github.com/SeisSol>), an open-source code based on the arbitrary high-order accurate derivative discontinuous Galerkin (ADER-DG) method (Dumbser & Käser, 2006) with end-to-end optimization for HPC infrastructure (e.g., Rettenberger et al., 2016; Uphoff et al., 2017b; Krenz et al., 2021). SeisSol uses fully non-uniform unstructured tetrahedral meshes that can statically adapt to complex 3D subsurface structures and topography. We create 3D tetrahedral meshes for the simulations using velocity-aware meshing, i.e., automatically adapting SeisSol’s mesh resolution to the 1D or 3D velocity model (Figure 2b). We ensure sufficient resolution using four elements with basis functions of polynomial degree of 4 per shortest wavelength (Käser et al., 2008). To inform the 3D models, we obtain the CVM-H velocity model using the SCEC UCVM software (Small et al., 2017). We obtain the topography data from the 1-meter resolution digital elevation model from the U.S. Geological Survey 3D Elevation Program (see data availability statement). We create the meshes with Gmsh (Geuzaine & Remacle, 2009), resulting in 550,001 tetrahedral elements for LOH, 129,888 elements for 3D-1400, and 1,189,840

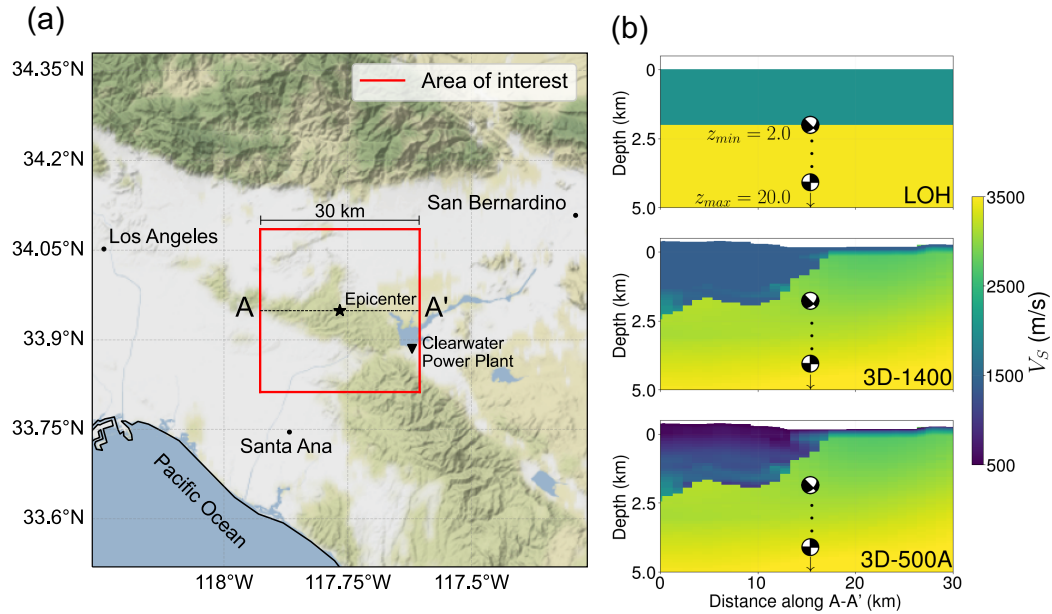


Figure 2: (a) Map of the area of interest (red box) and the surrounding region in Southern California. The epicenter of the simulated earthquakes (which is the same as the 2008  $M_w$  5.4 Chino Hills earthquake) is indicated by a black star and a site of interest is indicated by a black triangle. (b) Cross-sections (A - A') of the velocity models used for wave propagation simulation of the three forward models (LOH, 3D-1400, and 3D-500A). Note that the cross-sections correspond to the area of interest, though our simulations use larger meshes to prevent any potential spurious boundary reflections. As shown in the cross-sections, we vary the source depth and focal mechanism for each of the  $n_s = 5000$  simulations. The source depths range between  $z_{min}=2.0$  km and  $z_{max}=20.0$  km, though the cross-sections show a maximum depth of 5.0 km to better show the near-surface velocity structures.

elements for 3D-500A. All simulations were performed using a degree four polynomial in space and time (translating to a fifth-order accurate scheme in space and time) and were executed on SuperMUC-NG using 17 compute nodes. Each compute node consists of 48 cores employing Intel Skylake Xeon Platinum 8174 processors. Using these resources the runtimes per simulation were 59.5 s, 23.0 s, and 390.0 s for the LOH, 3D-1400, and 3D-500A models, respectively. Assuming perfect utilization of the  $17 \times 48$  cores, these runtimes translate to 13.5, 5.2, and 88.4 CPUh. We save the three-component free-surface velocity time-series for  $n_r = 3600$  receivers with a spacing of 500 m and sampling rate of 10.0 Hz. To create a ground motion map for each earthquake source, the last step is to compute the PGV from the time series of the horizontal components. We demean, detrend, and apply a 1.0 Hz lowpass filter to the time series before combining the two horizontal components using the orientation-independent RotD50 measure (Boore, 2010).

### 2.3 Reduced-order model

We now describe in detail how to define the ROM that approximates the mapping between the parameters  $\mathbf{p}$  and the PGV map  $\mathbf{q}$ .

#### 2.3.1 Parameter space sampling

To inform the ROM, we first select the points in the parameter space  $\mathcal{P}$  where we will obtain the FOM solutions. To determine these points, we use a low-discrepancy, four-dimensional Halton sequence (Halton, 1960). The low-discrepancy property of this sequence means that it closely approximates points drawn from a uniform distribution, giving us points that evenly cover our entire parameter space. We use the first  $n_s = 5000$  points from this sequence, where  $n_s$  is the total number of earthquake sources for which we evaluate the FOM. We gather the parameters determined by the Halton sequence into a matrix  $\mathbf{P} = [\mathbf{p}_1, \mathbf{p}_2, \dots, \mathbf{p}_{n_s}]$  and the PGV data generated by the FOM into a matrix  $\mathbf{Q} = [\mathbf{q}_1, \mathbf{q}_2, \dots, \mathbf{q}_{n_s}]$ . Generating the simulation data matrix  $\mathbf{Q}$  for  $n_s = 5000$  sources requires a total of 67.5 kCPUh, 26 kCPUh, and 442 kCPUh for the LOH, 3D-1400 and 3D-500A forward models, respectively. To create independent datasets for training and testing of the ROM, we randomly separate the PGV maps (stacked in  $\mathbf{Q}$ ) that result from these sources into training ( $\mathbf{Q}_{\text{train}}, \mathbf{P}_{\text{train}}$ ) and testing ( $\mathbf{Q}_{\text{test}}, \mathbf{P}_{\text{test}}$ ) datasets, where the testing dataset contains 10% of the simulated PGV maps ( $n_{\text{train}} = 4500$ ,  $n_{\text{test}} = 500$ ). The accuracy of the trained ROM can then be evaluated using PGV maps from the independent testing dataset.

As the goal of the ROM is to interpolate the known PGV maps for new sources in  $\mathcal{P}$  that we did not simulate, we measure the Euclidean distances between each testing parameter  $\mathbf{p} \in \mathbf{P}_{\text{test}}$  and its nearest-neighboring training parameter  $\mathbf{p}_{\text{nearest}} \in \mathbf{P}_{\text{train}}$ , i.e.,

$$d_{\text{nearest}}(\mathbf{p}) = \|\mathbf{p} - \mathbf{p}_{\text{nearest}}\|_2.$$

These are the distances after normalizing each dimension of the parameter space (depth, strike, dip, and rake) to range between 0 and 1. In our testing dataset, the distribution of distances has a mean value of 0.09 (Figure S1). We also create a set of sources  $\mathbf{P}_{\text{uniform}}$

that contains  $10^6$  uniformly distributed sources that evenly cover  $\mathcal{P}$ . While it is not possible to evaluate the FOM to obtain error estimates for the  $10^6$  points in  $\mathbf{P}_{\text{uniform}}$ , we show that our testing distribution is a good proxy of the errors as indicated by the mean and standard deviations of the distances for both  $\mathbf{P}_{\text{test}}$  and  $\mathbf{P}_{\text{uniform}}$  (Figure S1). For any earthquake source contained in  $\mathcal{P}$ , the distance to the nearest training point will be, on average, 0.08. The maximum possible distance to any training FOM location is 0.17 units which is our reported “fill distance” (De Marchi & Schaback, 2010) for our sampled FOM locations.

### 2.3.2 Interpolated proper orthogonal decomposition (iPOD)

We use a method for defining a ROM called the interpolated proper orthogonal decomposition (iPOD) (e.g., Bui-Thanh et al., 2003; Druault et al., 2005). In this technique (Figure 3a), we first compute a modal decomposition for the collected data using the singular value decomposition (SVD),

$$\mathbf{Q} = \mathbf{U}\mathbf{\Sigma}\mathbf{V}^T, \quad (1)$$

where  $\mathbf{U} = [\mathbf{u}_1, \dots, \mathbf{u}_{n_s}]$  contains the left singular vectors (or modes)  $\mathbf{u}_i$ ,  $\mathbf{\Sigma} = \text{diag}[\sigma_1, \dots, \sigma_{n_s}]$  is a diagonal matrix containing the singular values  $\sigma_i$ , and  $\mathbf{V}$  contains the right singular vectors (Berkooz et al., 1993). We then define the matrix of POD coefficients  $\mathbf{A}$  to be,

$$\mathbf{A}^T = \mathbf{\Sigma}\mathbf{V}^T \quad (2)$$

$$\mathbf{A} = \mathbf{V}\mathbf{\Sigma}, \quad (3)$$

where we denote individual entries of  $\mathbf{A}$  as  $\alpha_{ij}$ . Using Eqs. (1) and (3) we can express every  $\mathbf{q}_i \in \mathbf{Q}$  using a weighted sum (Figure 3a) of the left singular vectors, i.e.,

$$\mathbf{q}(\mathbf{p}_i) = \mathbf{q}_i = \sum_{j=1}^{n_s} \alpha_{ij} \mathbf{u}_j. \quad (4)$$

Eq. (4) is a restatement of the factorization defined in Eq. (1) and thus can only be used to reconstruct values of  $\mathbf{q}$  for parameters  $\mathbf{p} \in \mathbf{P}$ . To enable predictions for parameters  $\mathbf{p} \notin \mathbf{P}$ , the iPOD method utilizes a generalization of Eq. (4)

$$\mathbf{q}(\mathbf{p}) \approx \tilde{\mathbf{q}}(\mathbf{p}) = \sum_{j=1}^{n_s} f_j(\mathbf{p}) \mathbf{u}_j, \quad (5)$$

where each function  $f_j(\mathbf{p})$ ,  $j = 1, \dots, n_s$  predicts the POD coefficient for any parameter  $\mathbf{p}$  associated with the  $j^{\text{th}}$  mode (Figure 3b). The types of functions  $f_j(\cdot)$  that we consider are described in Section 2.3. After fitting the functions  $f_j(\mathbf{p})$  with the POD coefficients given by  $\alpha_{ij}$ , the PGV map  $\tilde{\mathbf{q}}$  is obtained by evaluating Eq. (5). In essence, iPOD builds an orthogonal basis  $\mathbf{u}_i$  based on simulation data ( $\mathbf{Q}$ ) with which it will use to define a predicted PGV map. The basis  $\mathbf{u}_i$  are combined linearly, with the associated weight of each basis defined by a functional approximation of the coefficients  $\mathbf{A}$ . The POD coefficients needed to reconstruct the training dataset are then given by  $\mathbf{A}_{\text{train}}$ .

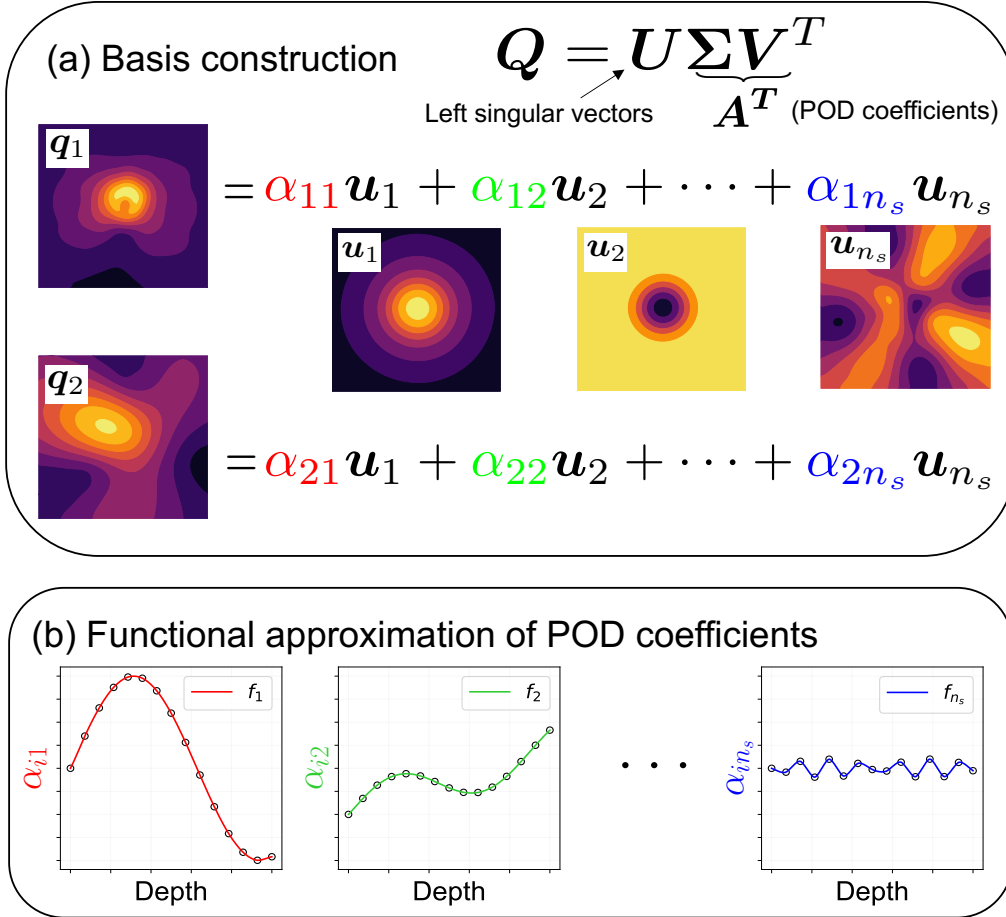


Figure 3: Conceptual illustration of a reduced-order model based on interpolated proper orthogonal decomposition (iPOD). We first decompose the data matrix of PGV maps  $Q$  using the singular value decomposition (a). The goal is then to fit a series of functions  $f_j$  (b) that predict the proper orthogonal decomposition (POD) coefficients  $\alpha_{ij}$  for different values of the input source parameters (e.g., hypocentral depth). The ROM-predicted PGV maps are obtained by evaluating the functions to obtain predicted POD coefficients, and then performing a weighted sum of the left singular vectors  $u_j$ .

### 2.3.3 Function approximation for $\alpha_{ij}$

We consider four types of function approximators to model the relationships between the source parameters  $\mathbf{p}$  and POD coefficients  $\alpha_{ij}$ . These include radial basis functions, neural networks, random forests, and  $k$ -nearest neighbors. We summarize these function approximation techniques below.

1. Radial basis function (RBF) interpolation is commonly used as an efficient technique for interpolating high-dimensional, unstructured data (Lazzaro & Montefusco, 2002) and has been shown to be successful in other studies that use iPOD (e.g., Audouze et al., 2009; Xiao et al., 2015). For RBF interpolation, the interpolator for the  $j$ -th mode  $f_j(\cdot)$  is given by

$$f_j(\mathbf{p}) = \sum_{i=1}^{n_{\text{train}}} w_{ij} \varphi(\|\mathbf{p} - \mathbf{p}_i\|) + \sum_{k=1}^{|V|} b_{kj} \psi_k(\mathbf{p}) \quad (6)$$

where the function  $\varphi(\cdot)$  is an RBF,  $w_{ij}$  is an entry of the kernel weight matrix  $\mathbf{W}$ ,  $b_{kj}$  is an entry of the polynomial coefficient matrix  $\mathbf{B}$ , and  $\psi_k(\cdot)$  are monomial terms up to a specified degree  $d$  contained in the set  $V$  with

$$V = \left\{ p_1^q p_2^r p_3^s p_4^t : \begin{cases} q + r + s + t \leq d \\ 0 \leq q, r, s, t \leq d \end{cases} \right\} \quad (7)$$

where  $p_1$  denotes the hypocentral depth,  $p_2$  denotes the strike, etc. We determine the coefficients contained in  $\mathbf{W}$  and  $\mathbf{B}$  by solving the linear system of equations

$$\begin{aligned} \Phi \mathbf{W} + \Psi \mathbf{B} &= \mathbf{A}_{\text{train}} \\ \Psi^T \mathbf{B} &= \mathbf{0} \end{aligned}$$

where

$$\Phi = \begin{bmatrix} \varphi(\|\mathbf{p}_1 - \mathbf{p}_1\|) & \varphi(\|\mathbf{p}_2 - \mathbf{p}_1\|) & \dots & \varphi(\|\mathbf{p}_{n_{\text{train}}} - \mathbf{p}_1\|) \\ \varphi(\|\mathbf{p}_1 - \mathbf{p}_2\|) & \varphi(\|\mathbf{p}_2 - \mathbf{p}_2\|) & \dots & \varphi(\|\mathbf{p}_{n_{\text{train}}} - \mathbf{p}_2\|) \\ \vdots & \vdots & \ddots & \vdots \\ \varphi(\|\mathbf{p}_1 - \mathbf{p}_{n_{\text{train}}}\|) & \varphi(\|\mathbf{p}_2 - \mathbf{p}_{n_{\text{train}}}\|) & \dots & \varphi(\|\mathbf{p}_{n_{\text{train}}} - \mathbf{p}_{n_{\text{train}}}\|) \end{bmatrix} \quad (8)$$

and  $\Psi$  is the matrix of polynomials up to degree  $d$ . For the RBFs  $\varphi(\cdot)$ , we test three types of kernels: thin plate spline ( $\varphi(r) = r^2 \ln(r)$ ), cubic ( $\varphi(r) = r^3$ ) and quintic ( $\varphi(r) = -r^5$ ). For each kernel, we solve the linear system using the minimum polynomial degree (equal to one for the thin plate spline and cubic kernels, and degree two for the quintic kernel). Note that we do not apply smoothing, which implies that the POD coefficients are exactly reproduced for the training dataset, i.e., for any  $\mathbf{p} \in \mathbf{P}_{\text{train}}$ . The type of RBF kernel (i.e., thin plate spline, cubic or quintic) is a hyperparameter that we tune using cross-validation.

2. Artificial neural networks are another type of function approximator for the POD coefficients (Hinton, 1990; Hesthaven & Ubbiali, 2018). We use a fully connected, feed-forward structure in which the neural network consists of an input layer, two hidden layers, and an output layer. This type of structure is also known as a multilayer perceptron (MLP). In this type of model, the input layer receives the four

- earthquake source parameters from  $\mathbf{p}$ , and the output layer returns the predicted POD coefficients. Each neuron in the hidden layers receives an input from each neuron in the previous layer, evaluates an activation function (ReLU), then passes the information forward through the network to every neuron in the next layer using determined weights and biases. We optimize the weights and biases by training the neural networks with the Adam optimizer (Kingma & Ba, 2017) and the squared error loss function. Furthermore, we follow the method of Swischuk et al. (2019) to predict a subset of the POD coefficients which correspond to the  $r$  largest singular values, choosing to train the neural networks using  $r = 10, 30,$  and  $50$  modes from the SVD (Eq. (1)). The hyperparameters for MLP consist of the rank  $r$  and the number of neurons in each hidden layer.
3. Random forests (RF) are a type of ensemble estimator in which many decision trees are constructed, and the final estimate is the mean of each decision tree’s individual estimate (Breiman, 2001). We here use both 50 and 100 decision trees. The hyperparameters are given by the number of decision trees.
  4.  $k$ -nearest neighbors (kNN) is a relatively simple type of approximator in which the predicted value is given as the mean of the  $k$ -nearest neighboring points. We apply uniform weighting to each point in the neighborhood and use the  $\ell_2$  norm as the distance metric. We test using 3, 5, and 7 neighbors which define the hyperparameters.

### 2.3.4 Training procedure

Before training the function approximators RBF, MLP, RF, and kNN, we standardize both the inputs (earthquake source parameters,  $\mathbf{P}$ ) and outputs (POD coefficients,  $\mathbf{A}$ ) such that they have a mean of zero and standard deviation of one. Note that we use all available modes (i.e., all columns of  $\mathbf{A}$ ) to train the ROMs, except for the MLP approximator where we allow the number of modes to be a hyperparameter. To determine the values of the hyperparameters, we use  $k$ -fold cross-validation with  $k = 5$ . In this procedure, the training dataset is further subdivided into 5 folds. For each of the folds, the remaining  $k-1$  folds are used to train the approximators, and the fold that was not included is the validation dataset. To measure the error of a ROM with a given set of hyperparameters, we use both the mean absolute error and the mean absolute percentage error. We define the local (in parameter space) mean absolute error as

$$MAE(\mathbf{p}) = \frac{1}{n_r} \|\mathbf{q}(\mathbf{p}) - \tilde{\mathbf{q}}(\mathbf{p})\|_1 \quad (9)$$

and the local mean absolute percentage error as

$$MAPE(\mathbf{p}) = \frac{1}{n_r} \left\| \frac{\mathbf{q}(\mathbf{p}) - \tilde{\mathbf{q}}(\mathbf{p})}{\mathbf{q}(\mathbf{p})} \right\|_1, \quad (10)$$

where  $n_r$  is the number of discrete points in space where the PGV map  $\mathbf{q}$  is defined. The average mean absolute error and average mean percentage error are obtained by average the local metrics over the discretely sampled parameter space  $\mathbf{P}_x$  and are defined

via

$$\overline{MAE}(\mathbf{P}_x) = \frac{1}{n_x} \sum_{i=1}^{n_x} MAE(\mathbf{p}_i) \quad (11)$$

$$\overline{MAPE}(\mathbf{P}_x) = \frac{1}{n_x} \sum_{i=1}^{n_x} MAPE(\mathbf{p}_i), \quad (12)$$

where  $\mathbf{p}_i \in \mathbf{P}_x$  and  $n_x = \text{card}(\mathbf{P}_x)$  is the number of parameter instances in the dataset  $\mathbf{P}_x$ . When performing cross-validation, we select the hyperparameters for each type of approximator that result in the lowest  $\overline{MAE}$  averaged across all five folds. We then re-train the approximators on the entire training dataset using the cross-validated hyperparameters and evaluate the  $\overline{MAE}$  and  $\overline{MAPE}$ , now on the completely independent testing dataset. Altogether, this process allows us to find the best-fitting ROMs while also giving us independent estimates of the ROM errors.

### 3 Results

#### 3.1 Information content of the proper orthogonal decomposition

After generating the simulation data matrix  $\mathbf{Q}$ , we first present the singular value distribution resulting from performing the SVD. The efficiency and applicability of a reduced-order model for a given physical problem is directly related to the singular value distribution. Ideally, the singular values will rapidly decay, implying that  $\mathbf{Q}$  has low-rank. To characterize the singular value distribution of  $\mathbf{Q}$  we use the relative information content (RIC) given by

$$\text{RIC}(r) = \frac{\sum_{i=1}^r \sigma_i^2}{\sum_{i=1}^{n_s} \sigma_i^2},$$

where  $r$  is the number of modes (left singular vectors). Using  $\text{RIC}(r)$ , low-rank matrices will result in  $\text{RIC} \approx 1.0$  when  $r$  is small. Furthermore, the RIC may be used to guide the number of modes to use in defining the ROM (Swischuk et al., 2019), because the higher-order modes contribute little to the solution such that they may be truncated.

In our generated datasets for all three forward models (LOH, 3D-1400, and 3D-500A) using  $n_s = 5000$ , we find that only a few modes are necessary to capture a significant portion of the information content (Figure 4). Specifically, only 13 modes are required to recover 99% of the information content for the data generated by LOH, 17 modes are required for 3D-1400, and 20 modes are required for 3D-500A. These results indicate that the simulated PGV maps, independent of the forward model complexity, all have low-rank. Since the number of modes reached to capture 99% of the information within  $\mathbf{Q}$  is only slightly larger for 3D velocity model setups, this suggests that the PGV-based ROM may be only slightly more difficult to approximate (i.e., less accurate) compared to the PGV maps associated with LOH.

#### 3.2 Quantitative comparison of function approximators

Here, we present the results of training the ROMs using different types of function approximators. In particular, we investigate the errors between the ROM predictions and

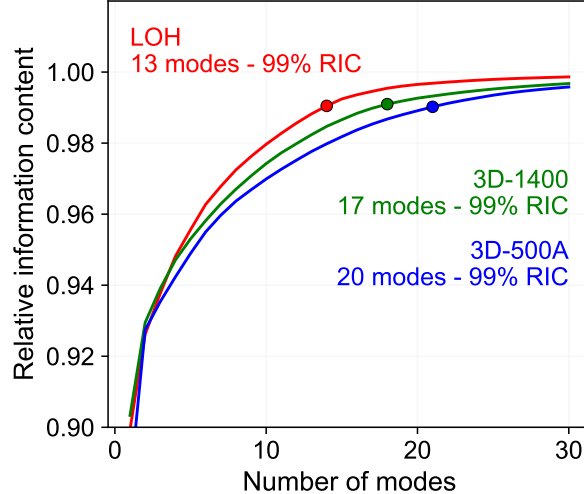


Figure 4: Relative information content (RIC) plotted as a function of the number of modes for the 5000 simulated PGV maps produced by the forward models (LOH in red, and 3D-1400 in green, 3D-500A in blue). Note that the horizontal axis is limited to show only the first 30 modes. We illustrate this result in a movie (Movie S1) that shows PGV maps defined using an increasing amount of  $r$  left singular vectors, where we observe that the maps are well-approximated by the first few modes.

the simulated PGV maps in the testing dataset. We examine how the ROM errors change depending on the amount of training data. We train the ROMs with increments of  $n_s/5$  forward models and determine the cross-validated hyperparameters for each approximator as described in Section 2.3. For each approximator, we show the errors (both  $\overline{MAE}$  and  $\overline{MAPE}$ ) corresponding to the hyperparameters that result in the lowest  $\overline{MAE}$  (Figure 5). We indicate the hyperparameters that were selected for the final evaluation of each approximator using  $n_s$  forward models in Table S2.

Figure 5 shows that all approximators generally result in ROMs with lower error as more simulations are added to the training dataset. We observe that the RBF-based ROM consistently has the lowest error out of all ROMs that we consider, a result that is independent of the type of velocity model (either 1D or 3D). When trained with the complete set of training data, the RBF-based ROM performs with an average absolute PGV error of  $\overline{MAE} = 0.07$  cm/s for the LOH forward model,  $\overline{MAE} = 0.09$  cm/s for 3D-1400, and  $\overline{MAE} = 0.11$  cm/s for 3D-500A. The approximate values for  $\overline{MAPE}$  are 7%, 8%, and 8%, respectively. The local slope of the error curves, especially for  $\overline{MAE}$  are variable as  $n_s$  increases. Specifically for  $n_s = 3000$ , we observe that the local slope for  $\overline{MAE}$  is approximately zero, and for all but the RBF interpolator is actually positive. This indicates that some points in the parameter space which are being sampled are not particularly informative for the ROM. However, for higher values of  $n_s$ , the continuing downward slope of  $\overline{MAPE}$  for the RBF-based ROM suggests that additional training data might further decrease the ROM errors. Similar trends are observed for all ap-

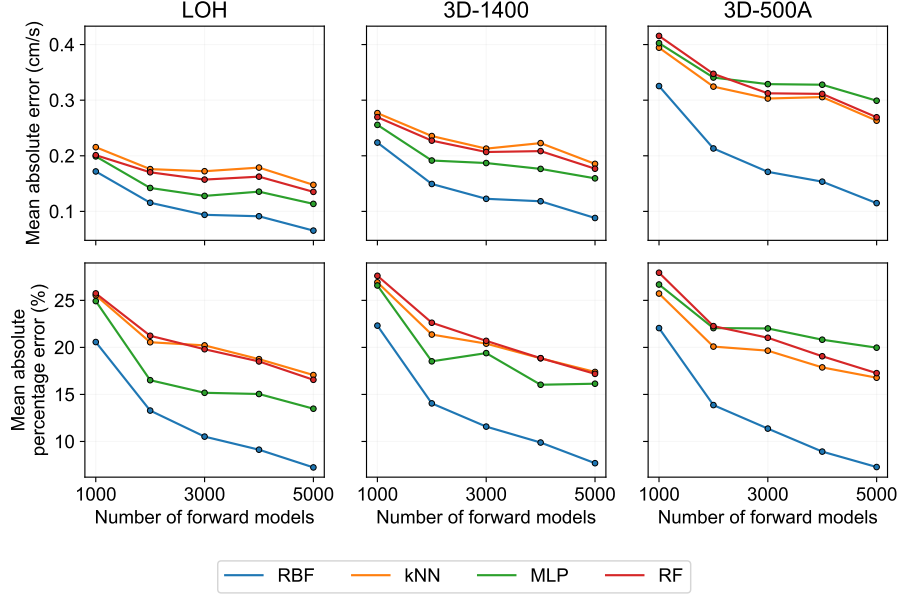


Figure 5:  $\overline{MAE}$  (top row) and  $\overline{MAPE}$  (bottom row) errors for the different ROMs using the LOH (left column) and 3D-1400 (right column) forward models. Each approximator is shown with a different colored solid line (see legend). For each number of forward models ( $n_s$ ), we evaluate the errors using the testing dataset and the best hyperparameters selected from 5-fold cross-validation (see Table S2 for the selected hyperparameters). The mean values of  $d_{\text{nearest}}$  for the testing datasets are 0.13, 0.11, 0.10, 0.09, and 0.09 for the evaluations made using 1000, 2000, 3000, 4000, and 5000 forward models, respectively.

proximators with LOH across both error metrics. Additionally, the slope of the lines in going from  $n_s = 4000$  to 5000 is approximately the same across all approximators. The same observations are observed for 3D-1400, with the exception of the MLP approximator. MLP exhibits a smaller slope for large values of  $n_s$  in  $\overline{MAE}$  and an approximately zero slope in  $\overline{MAPE}$  when  $n_s$  increases from 4000 to 5000.

In addition to examining the overall errors on the testing dataset, it is informative to examine spatial errors within the PGV maps. We show examples of simulated PGV maps created using all three velocity models, the predictions from the four types of approximators, and map-views of the errors (Figure 6). The map views of the errors illustrate locations in which the ROM produced accurate PGV estimates, or where the PGV was over/under-predicted. For the specific earthquake source in this example with oblique slip, the PGV is strongest a few km northwest of the epicenter, with simulated PGVs reaching up to 12.0 cm/s for the 3D-500A setup. Averaged across all receivers, the RBF ROM gives the smallest error ( $MAE=0.07$  cm/s for LOH), while the kNN ROM gives the largest error ( $MAE=0.18$  cm/s).

Although the errors show significant differences depending on the type of function approximator, each approximator generally reproduces the overall spatial distribution

and amplitudes of the forward model ground motion map. The RBF interpolator does significantly better in correctly predicting ground motions in the areas of strongest and weakest shaking. Notably, the errors for the RBF ROM are near zero where the shaking is the strongest. The other approximators share some common problems, such as over-prediction at the eastern edge of the domain and under-prediction near the southwest. The kNN, in particular, tends to overestimate the PGVs in the near-epicentral area of strong shaking. Overall, we conclude that the RBF ROM performs exceptionally well at recovering the spatial distribution of ground motion compared to the other approximators.

### 3.3 ROM solutions for different sources

We next demonstrate the ROM’s ability to predict the changes in the spatial patterns and amplitudes of peak ground motions when the hypocentral depth and focal mechanism of the earthquake source are subject to change. We show examples of PGV maps created with the LOH velocity model using three different sources from the independent testing dataset (Figure 7). The PGV maps that result from the same sources for the 3D-1400 forward model are shown in Figure 8, and the maps for 3D-500A are shown in Figure 9. In these figures, we select three sources in  $\mathcal{P}_{\text{test}}$  where the distance  $d_{\text{nearest}}$  is close to the expected value (0.09) of the distribution of distances for any source in  $\mathcal{P}$ . We simplify the presentation by only showing the RBF interpolator results, as this is our preferred function approximator for the ROM. As the source focal mechanism changes, we see the ROM correctly reproduces the changes that occur to the PGV map.

We see that the physically more complex forward models 3D-1400 and 3D-500A produce more complex spatial PGV distributions, compared to the much smoother distributions produced by the simpler LOH models. Comparing Figures 7 & 8, the ROM for 3D-1400 has only slightly more difficulty in predicting the smaller-scale features in the 3D-1400 data, and the errors are only slightly larger compared to LOH. These small differences between LOH and 3D-1400 are consistent with the overall trends from the testing dataset. Comparing 3D-1400 against 3D-500A, we see that 3D-500A results in larger PGVs due to the slower wave speeds included in the velocity model. For these particular sources, the MAE values are about 2.0 times larger for 3D-1400 compared to 3D-500A. The complete set of error measurements on the testing dataset are shown as histograms in Figures S4 and S5, respectively, for the three forward modeling setups.

We inspect the accuracy of the ROMs for different values of the input source parameters. In Figure 10, we show the average and standard deviation of  $MAE$  for 20 evenly spaced bins for each of the four source parameters. For all three forward models, we observe that the shallower events show larger errors compared to deeper events. This is partially explained by the larger PGVs expected for shallow sources, although the relative  $MAPE$  errors show a non-negligible correlation with hypocentral depth (Figure S7). There is more variability in the errors for shallow events compared to deep events as indicated by the standard deviations. Shallow sources introduce additional near-source effects to ground shaking which may be underrepresented in the training dataset following using

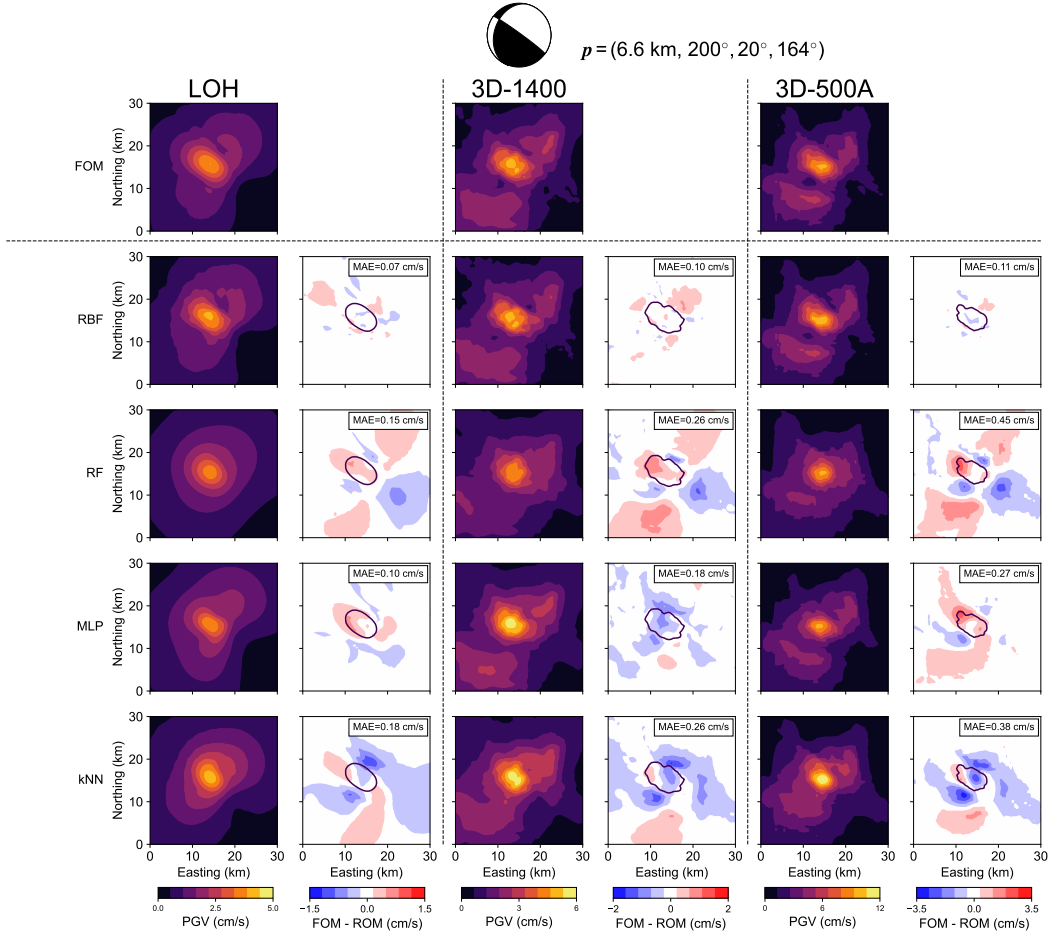


Figure 6: Comparison of the ROM solutions using different function approximators for a single earthquake source (focal mechanism shown in the first row). The second row shows the target PGV maps for LOH (left) and 3D-1400 (right). The subsequent panels show the ROM predictions and errors, where each row is for a different approximator (see row labels at left). The approximators are sorted from lowest to highest error (top to bottom), and each error map is indicated with the  $MAE$  in the top right corner. The error maps outline the areas of strongest FOM shaking where the PGV is 90% of the largest PGV produced by each FOM.

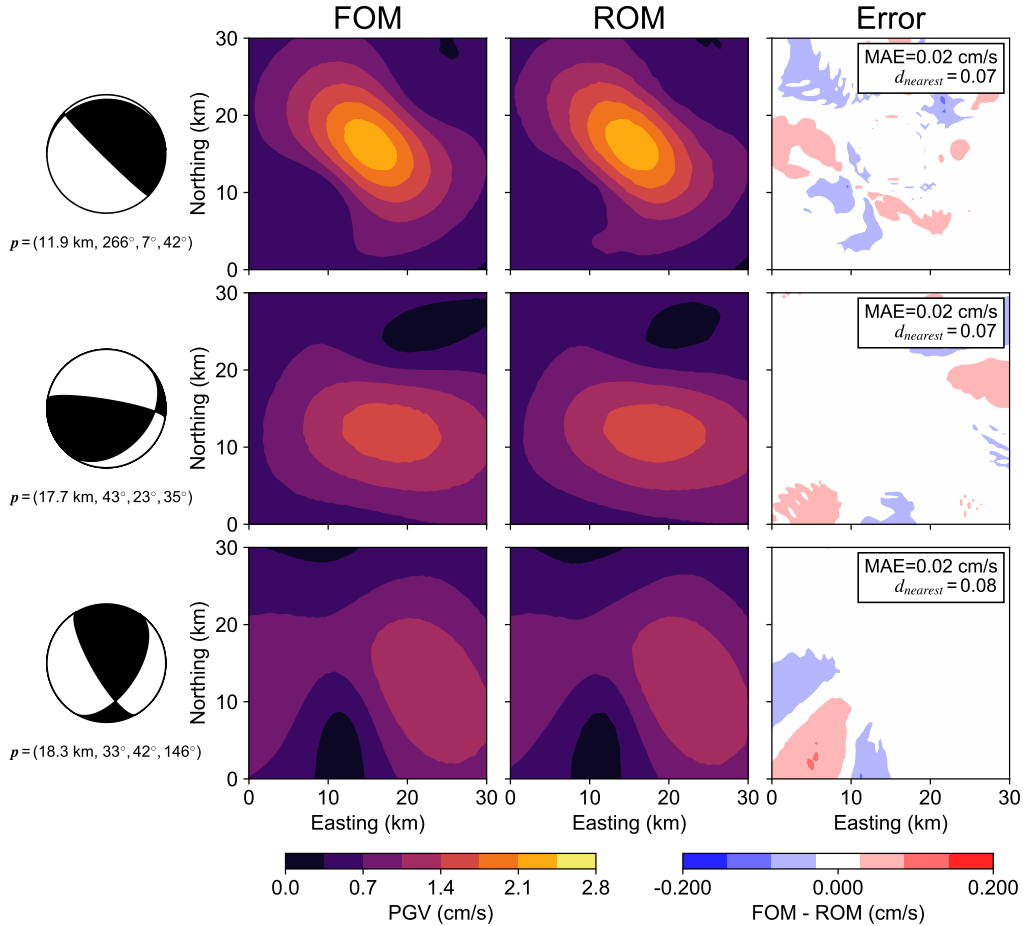


Figure 7: Plots of three simulated PGV maps (second column), RBF ROM predictions (third column), and errors (fourth column) for the LOH forward model. Each row indicates the results for a different earthquake source in the testing dataset, where the source parameters are indicated by the focal mechanisms in the first column. The error maps show the difference between the FOM and ROM solutions, and indicate the mean absolute error (MAE) and distance to the nearest training location ( $d_{\text{nearest}}$ ). The complete set of errors on the testing data can be viewed as histograms in Figures S4 and S5.

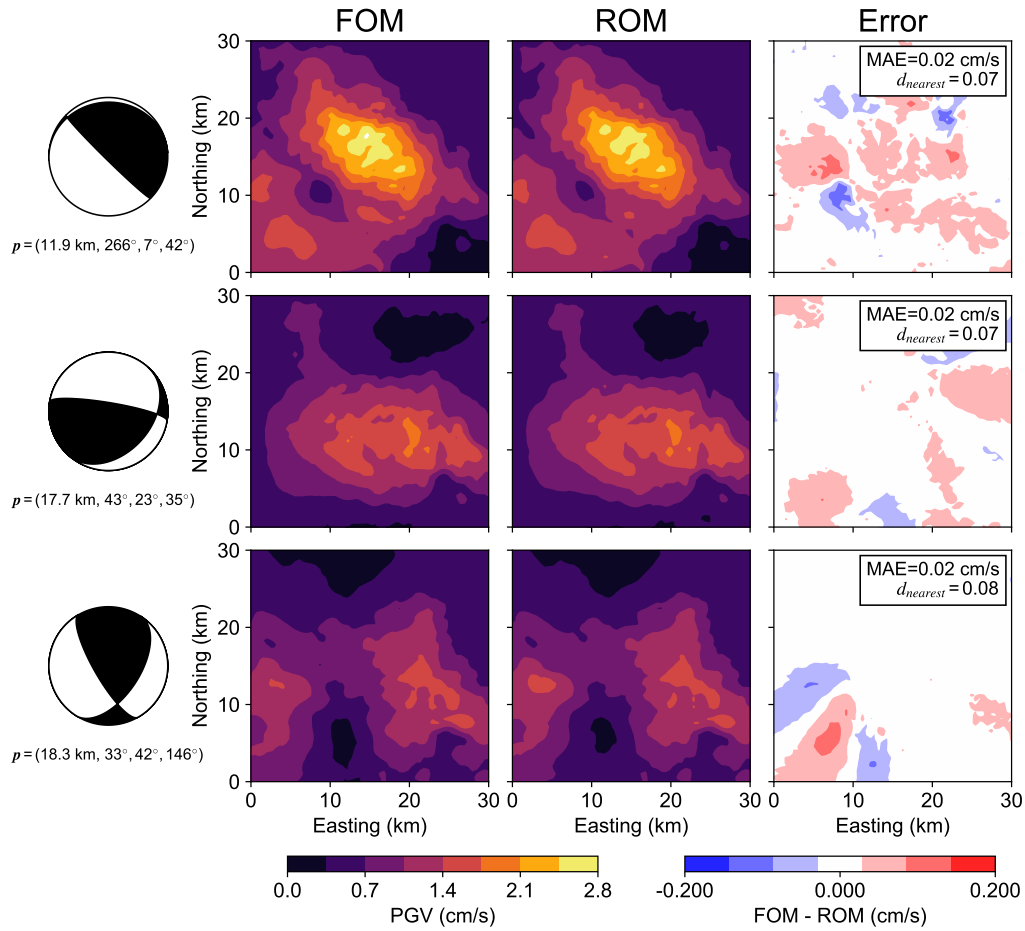


Figure 8: Plots of the simulated PGV maps, ROM predictions, and ROM errors for the same sources as shown in Figure 7, but shown here for the 3D-1400 forward model. The forward model includes 3D velocity structure (with minimum S-wave speeds of 1400 m/s) and topography.

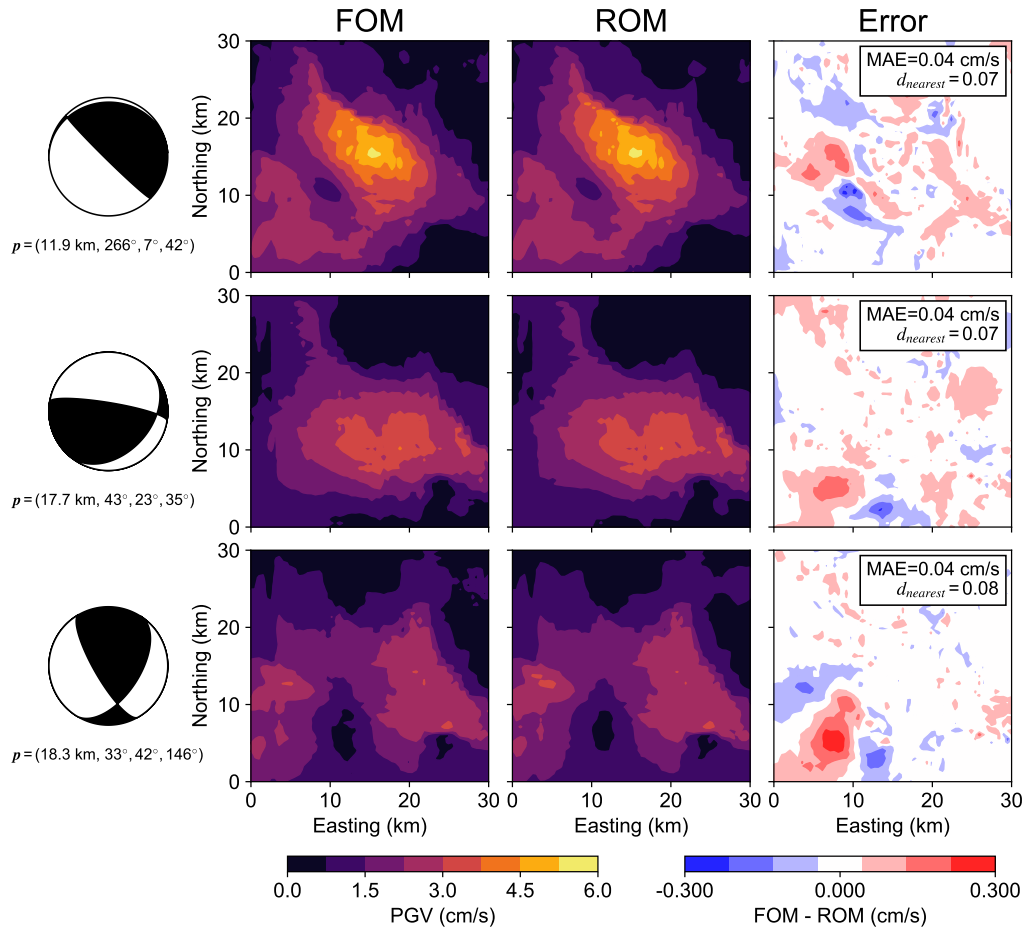


Figure 9: Plots of the simulated PGV maps, ROM predictions, and ROM errors for the same sources as shown in Figure 7, but shown here for the 3D-500A forward model. The forward model includes 3D velocity structure (with minimum S-wave speeds of 500 m/s), topography, and 3D variable viscoelastic attenuation.

our uniform sampling strategy. For the other source parameters related to geometry (i.e., focal mechanism, parameterized as strike, dip, and rake), the errors do not show significant correlations. The standard deviations in each bin are larger for these parameters, indicating that the ROM errors are primarily controlled by the source hypocentral depth. Overall, these results imply that the ROM errors are less dependent on the focal mechanism than on the source hypocentral depth.

### 3.4 Relationship between ROM errors and distance to training locations

It is reasonable to expect that the ROM errors will be smaller for the testing parameters that have a closer neighbor in the training dataset (i.e., a smaller value for  $d_{\text{nearest}}$ ). We indeed see this trend for our testing dataset (Figure S2) where the errors correlate with the distance to the nearest neighbor. The largest error of  $MAE_i \approx 0.8$  cm/s (for 3D-1400) occurs when the distance between the testing parameter and the nearest training parameter is approximately equal to the fill distance of 0.17. When the Euclidean distance  $d_{\text{nearest}}$  increases beyond 0.12 units, the error becomes significantly larger indicating that the interpolation quality of the ROM degrades when the distance to the nearest training point is too large. This relationship between  $d_{\text{nearest}}$  and ROM error can be used to estimate ROM errors for earthquake sources contained in  $\mathcal{P}$  where we do not have a FOM solution. For example, for an earthquake source with a parameter  $\mathbf{p}$  that is 0.1 distance units away from the nearest training FOM location, we expect the  $MAE_i$  of the ROM-predicted PGV map for 3D-1400 to be, on average, 0.1 cm/s.

To quantify the value added by the ROM, we examine the predicted PGV maps that would result from a simple approach of selecting the nearest-neighboring training FOM solution. As shown in Figure S3, the error for all forward models is about 2.5 times larger when selecting the nearest training FOM solution, compared to our preferred ROM estimates. This result illustrates that our ROMs are successfully interpolating between the training FOM solutions to obtain better estimates than could be obtained from just the simulated data.

### 3.5 Quantification of the effect of depth uncertainty on PGV predictions

We now present an exemplary application using the ROMs to study ground motion effects related to variable earthquake source parameters. In current operational earthquake early warning algorithms, the source focal depths are typically fixed at 8.0 or 10.0 km to minimize computational costs (Böse et al., 2018; Chung et al., 2019). These depth assumptions are reasonable in California where most earthquakes occur on shallow crustal faults (Brown et al., 2011) but may negatively affect alerting accuracy in other regions, for example, intraslab earthquakes in the Pacific Northwest (Thompson et al., 2022). With the ROMs, we can quantify the potential error that may be committed by an incorrect assumption of the hypocentral depth. We use our 3D-500A ROM to make predictions for 1 million different focal mechanisms, obtaining the PGV maps for both a shallow (2.0 km) and a deep (8.0 km) source. The focal mechanisms are obtained by sampling a uniform grid of 100 points along each of the three focal mechanism parameters. Using the

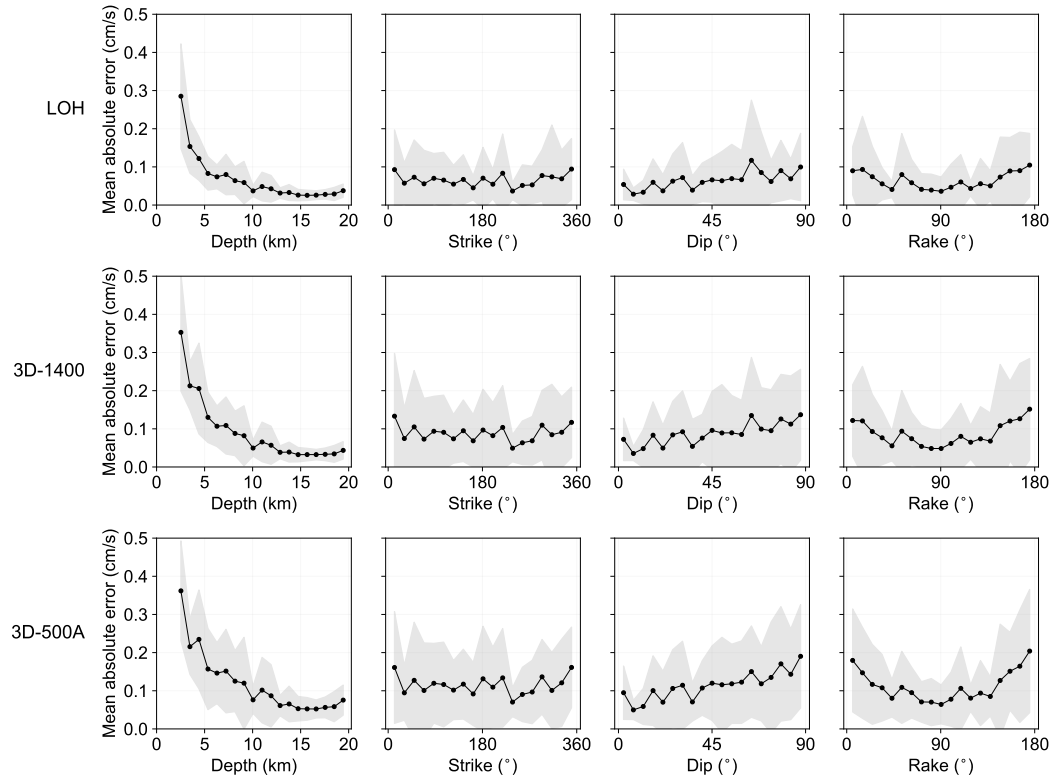


Figure 10: Mean absolute errors for the PGV predictions on the testing dataset, plotted as a function of each earthquake source parameter. LOH predictions are shown in the top row, and 3D-1400 predictions in the bottom row. For each parameter, we compute the mean (black line and dots) in 20 different evenly spaced bins and plot  $\pm 1.0$  standard deviation of the error in each bin (shaded area).

RBF ROM to create ground motion maps for these 2 million earthquakes requires  $\sim 1320$  s on a personal laptop<sup>1</sup>. This translates to a time-to-solution for a single earthquake scenario of  $\sim 0.66$  ms, or  $\sim 0.6 \times 10^{-6}$  CPUh<sup>2</sup>.

To simplify our analysis of ground motion variability related to the source parameters, we chose to focus on an individual site in our computational domain. We select the Clearwater Power Plant (33.891 N, 117.609 W) near the southeastern part of our domain (see Figure 2a). At this site, the ROM predictions show that the PGV varies significantly depending on the focal mechanism (Figure 11a). Averaging across all focal mechanisms, the mean difference in PGV between the shallow and deep sources is 1.8 cm/s; however, the maximum PGV difference is 3.6 cm/s for certain focal mechanisms. This result implies that, in the worst-case scenario, the PGV predictions based on an 8.0 km hypocentral depth could underestimate the true PGV at this site by up to 3.6 cm/s if the true hypocentral depth is 2.0 km.

One advantage of the ROM approach is that we can deterministically verify individual estimates by performing additional forward simulations. Here, we verify the ROM-based estimate for the worst-case scenario by performing two additional 3D-500A simulations (see Section 2.2) using the focal mechanism that resulted in the largest ROM-predicted PGV difference (between shallow and deep sources) at our site of interest. In the forward simulations, the PGV difference between the shallow and deep sources is 2.8 cm/s for the site. In comparison, the ROM-based estimate of the PGV difference is 3.6 cm/s. The discrepancy likely results from the ROM over-estimating the PGV for the shallow source. However, this amount of error is well within the expected error as indicated by the mean absolute errors from the testing dataset at this site (Figure S6). The amount of error for the ROM-estimated PGV differences (between shallow and deep sources) that are closer to the mean will be similar to the worst-case scenario because the errors are uncorrelated with the focal mechanism angles (Figure 10). Overall, this experiment highlights the potential in using ROMs to identify potentially damaging ground motions that might be overlooked when using a smaller sample size of physics-based simulations.

### 3.6 Sensitivity analysis using Pearson correlation coefficients

Finally, we analyze the correlations between variable earthquake source parameters and the PGV predictions at the same site of interest. This type of analysis allows us to quantify the relative importance of the model inputs (earthquake source parameters) with respect to the model output (PGV) (Homma & Saltelli, 1996). Here, we perform a global sensitivity analysis, which is closely related to the problem of forward uncertainty quantification (e.g., Pagani & Manzoni, 2021).

To measure the correlations, we again sample 1 million earthquakes, where the source parameters are randomly sampled from uniform distributions. After obtaining the ROM solutions at the Clearwater Power Plant for these sources, we measure the correlation

---

<sup>1</sup> MacBook Pro (2020), Intel(R) Core(TM) i5-1038NG7 CPU @ 2.00GHz

<sup>2</sup> As measured by the macOS application “Activity Monitor”

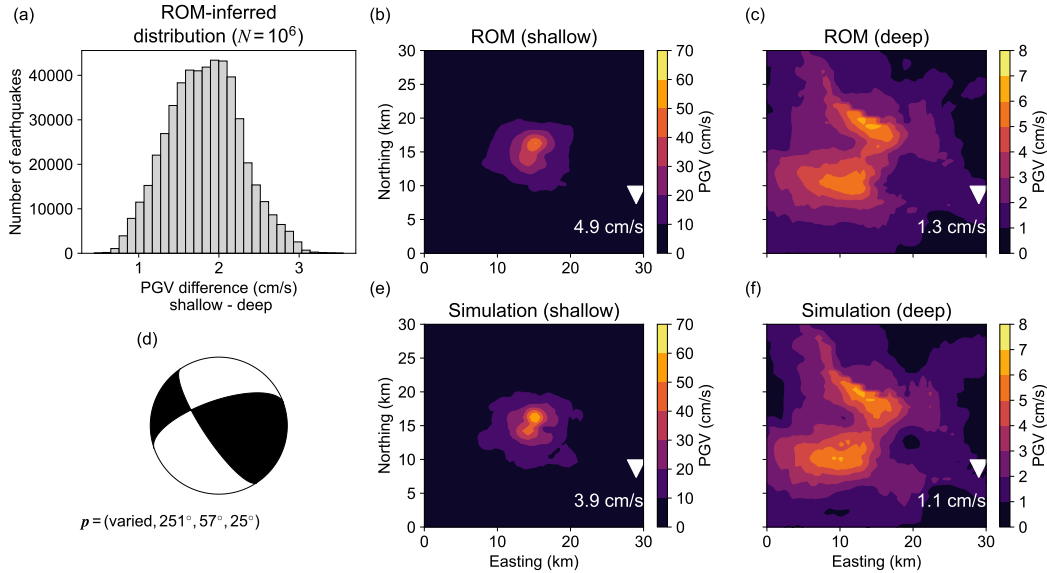


Figure 11: Histogram showing the distribution of differences between the shallow (2.0 km) and deep (8.0 km) source PGV predictions for 1 million different focal mechanisms (a). The ROM PGV predictions for the worst-case focal mechanism (d) are shown for the shallow source (b) and deep source (c). The corresponding simulations are shown in the bottom row in (e) and (f). In the PGV maps, the site of interest is indicated by a white triangle, and the site’s PGV value is printed.

between each source parameter and the PGV data using the Pearson correlation coefficient ( $r_p$ ) (Pearson, 1895). We find a significant inverse correlation ( $r_p = -0.65$ ) between the PGV predictions and hypocentral depth (Figure 12). For the focal mechanism angles, the correlation coefficients are near zero, implying that there is no consistent linear relationship between any of the focal mechanism parameters and PGV. However, there are features in the relationships between source parameters and PGV that cannot be adequately captured by the correlation coefficient. For example, the strike clearly affects PGV at this site by means of radiation pattern effects which cause the visible streaking patterns. Additionally, the kink in the PGV scaling with depth at about 5 km affects the correlation coefficient measurement. We note that these general correlations could also be measured from the PGV ground motions produced directly by the FOM (Figure S9), while the 1 million ROM predictions provide finer detail compared to solely examining the 5000 FOM measurements. Overall, while the PGV at a site of interest may vary significantly depending on the source parameters, the hypocentral depth is the most significant contributor to the PGV variability in our dataset. This finding agrees with the accuracy analysis presented in previous sections.

Lastly, we quantify our site of interest’s variability in PGV that results from changing the source focal mechanism. We consider this type of variability to be analogous to the inter-event terms that are often reported by GMMs which use mixed-effects regressions, such as ASK14 (Abrahamson et al., 2014). We bin our PGV data shown in Fig-

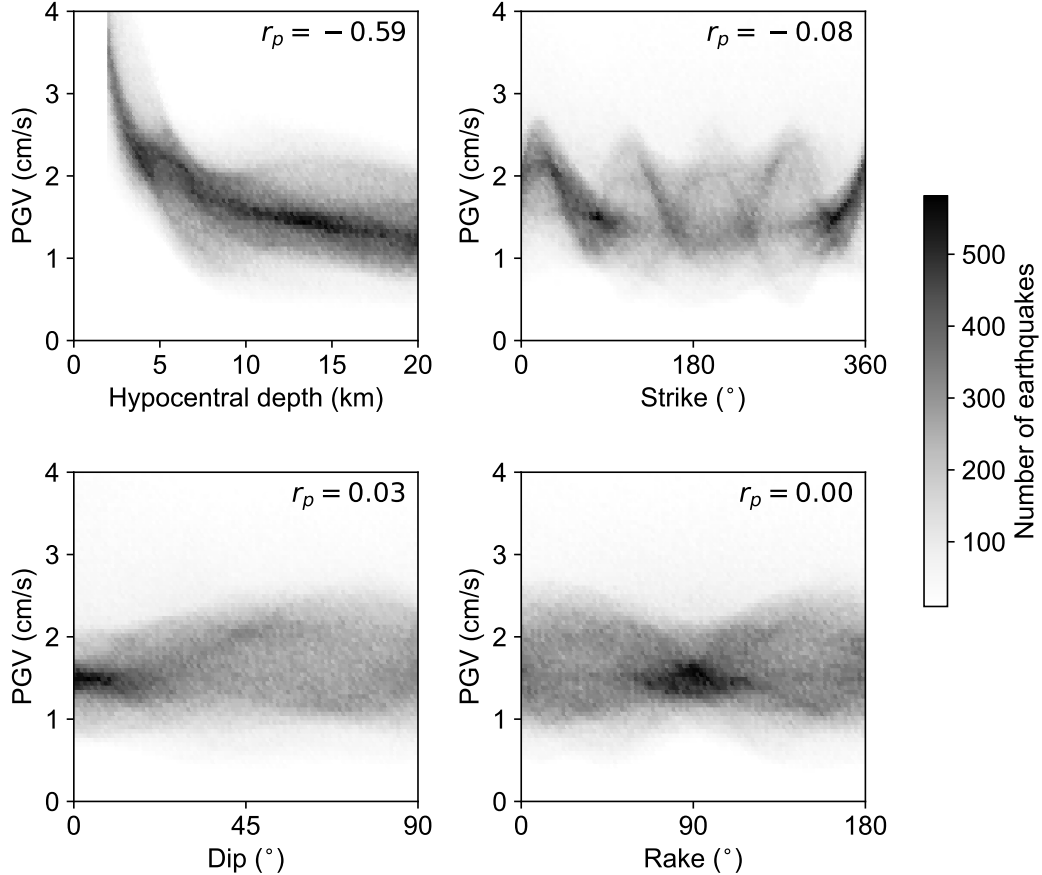


Figure 12: 2D density plots of the 3D-500A PGV predictions at the site of interest, plotted against each source parameter. In each bin, the number of earthquakes is indicated by the color bar to the right. The Pearson correlation coefficient is indicated in the top right of each panel.

ure 12 into 30 equally sized hypocentral depth bins and compute the mean and standard deviation for each bin. We find that the standard deviation increases for increasing hypocentral depths, and ranges from 0.18 to 0.32 natural log units (Figure S8). These variability measurements are somewhat lower compared to GMMs, for example ASK14, which reports an inter-event standard deviation of 0.38 natural log units for  $M_w = 5.4$ . This is an expected result, however, as the ROM-predicted PGV variability only accounts for variations in focal mechanism and not other source properties (e.g., stress drop) which increase the inter-event standard deviations in GMMs. We discuss this topic further in the following section.

#### 4 Discussion

We have constructed ROMs with the goal of predicting PGV maps for three different model setups of increasing complexity. We indeed find that the ROMs accurately

predict PGVs (about 0.1 cm/s average error) for both the 1D layer-over-halfspace (LOH) forward model and the 3D velocity models with topography (3D-1400 and 3D-500A) where the ROM errors are only slightly larger for the 3D velocity models. We find that the ROM approach works well for both linear elastic and viscoelastic forward models of seismic wave propagation, including low S-wave velocities, as shown by our results for the 3D-500A forward model. The ROM ground motion errors are not uniformly distributed across the parameter space, however, as the ROM errors tend to be larger (in both an absolute and relative sense) for shallow events compared to deep events. While this study uses a low-discrepancy Halton sequence to determine the FOM training data that inform the ROM, it may be beneficial in future ROMs to non-uniformly sample the parameter space. For example, we suspect the larger errors for shallow sources may result from the slower near-surface velocities which cause fewer training samples to be drawn per wavelength. As such, future ROMs might benefit from drawing the training FOM locations proportionally to the slowness in the velocity model, which would result in more training data for shallow sources compared to deep sources. The error for shallow sources could also be corrected using iterative ROM assembly (e.g., Lye et al., 2021) where the errors on the testing dataset are used to guide which new parameters will be sampled for the next iteration.

Future ROMs may investigate other function approximators beyond the four types we considered here. We find RBF interpolation to perform the best for our application of interest, while other studies have obtained good results using more generalized Gaussian process regression (Guo & Hesthaven, 2018). This approach may allow for more flexibility in the kernel length scales which can be optimized to better fit the data, as our RBF interpolation is essentially a special case of Gaussian process regression.

Using a Chino Hills earthquake scenario as our target simulation, we show that ROMs can be used as on-demand ground motion simulators for modeling wave propagation up to 1 Hz. This frequency target is consistent with the current understanding that PGV is controlled by frequencies around 1 Hz (e.g., Rodgers et al., 2020). However, the ROM predictions may under-estimate real PGV for smaller earthquakes which are enriched in higher frequency content. In addition, the minimum chosen  $V_S$  in our forward simulations does not account for materials with even slower wave speeds that cause ground motion amplification in specific regions, for example, the San Francisco Bay area muds (e.g., Hough et al., 1990). To generate rapid, physics-informed PGV maps targeted in these regions for earthquake engineering and seismic hazard applications, the amount of computing time spent in the FOM data collection phase would increase due to the higher cost of each forward simulation. For example, halving the minimum shear wave velocity (or doubling the resolved frequency) would require a factor of  $2^4 = 16$  higher computational cost (assuming spatially adaptive unstructured meshes and local time-stepping). However, we expect the ROM approach to be able to capture the changes to the PGV maps, as we show that there is little difference in the rank of the simulated data matrices when we lower  $V_{S,\min}$  from 1400 to 500 m/s. We suspect this would also be true if the simulations resolved higher frequencies and accounted for even slower near-surface wave speeds. ROM-based ground motion maps from higher-frequency and physically more

complex simulations (e.g., including approximations of linear and nonlinear site effects), may help to better understand source, path and site contributions to ground shaking (e.g., Hartzell et al., 1997; A. D. Frankel et al., 2002; Hashash & Park, 2002).

While the aim of this study is to demonstrate how the ROM approach can emulate a ground motion simulation scenario with variable source properties, we note in the following possible future extensions that may generalize the ROMs for ground motion prediction of real earthquakes with arbitrary source locations and magnitudes. For one, we expect the ROM approach will be applicable to forward models involving more realistic earthquake source representations, such as finite kinematic or dynamic rupture sources. In this study, we did not parameterize forward simulations with variable moment magnitudes. While our PGV maps could be scaled to represent different  $M_w$  using a magnitude-scaling term from GMMs, for example (Baltay & Hanks, 2014), the point-source approximation we use here omits finite source effects such as directivity (Spudich et al., 2014). We note that our simulations only consider a single epicentral location, and will not accurately predict the path effects in regions with different velocity structures. This issue may be investigated by extending  $\mathcal{P}$  to include latitude and longitude as additional source parameters, and we expect the ROM approach to be useful in that case to study basin or topographic effects that depend on the source-to-site azimuth (e.g., Thompson et al., 2020; Stone et al., 2022). Variations to our fixed source-time function would allow us to study variable stress drop, which has been shown to correlate with peak ground acceleration in observational datasets (Trugman & Shearer, 2018). Recorded ground motion observations are typically not available at the required density to build ROMs. While we here rely on physics-based simulations to obtain PGV maps, we expect that future work may incorporate sparse, observed ground motions into the ROM framework to provide additional constraints on the ground motion amplitudes and variability.

While finite earthquake source effects on PGVs may be readily included in ROMs with additional source parameters, an alternative approach is to predict Green’s functions instead of PGV maps. This would allow the ground motion intensities to be computed for arbitrary source-time functions, and allow for predictions using finite-fault sources using the superposition property of the elastic wave equation. However, this approach might be challenging if the Green’s functions do not possess low-rank structure like the PGV maps we predict in this study. For this application, deep learning and neural operator methods for time-dependent output quantities may be considered (e.g., Yang et al., 2021, 2023) though they have yet to be applied to 3D elastodynamic wave propagation in models that include topography. Future directions in instantaneous ground motion estimates may involve non-source-based approaches that use ROMs to forecast wave-field snapshots, either used simulated or observed data (e.g., Nagata et al., 2023).

## 5 Conclusion

We develop a reduced-order modeling (ROM) approach and use it to instantly create peak ground velocity (PGV) maps that closely match computationally expensive wave propagation simulations with variable source depth and focal mechanisms. We show that

the simulated PGV maps have low-rank structure which motivates our use of the interpolated proper orthogonal decomposition technique. The accuracies of the ROMs are similar when a 1D or 3D-velocity model (including topography, viscoelastic attenuation, and slow S-wave speeds) is used for the simulations of seismic wave propagation. We find that the ROM errors are primarily controlled by the hypocentral depth (larger errors for shallow sources). After comparing different approximation strategies with cross-validation, we find that radial basis function interpolation performs well, showing small (mean absolute PGV error  $< 0.1$  cm/s) errors on an independent testing dataset. We lastly demonstrate the potential of using ROMs to answer questions about ground motion variability that would ordinarily be computationally intractable when using full complexity forward simulations of wave propagation. We conclude that the reduced-order modeling approach defined via the interpolated proper orthogonal decomposition is a viable technique to obtain physics-informed estimates of the relationship between source properties and PGVs for ground motion simulation scenarios.

## 6 Open Research

### 6.1 Data Availability Statement

We use the Scikit-learn (Pedregosa et al., 2011) and SciPy (Virtanen et al., 2020) Python modules for their implementations of the approximators used in this study. We created the figures for this work using matplotlib (Hunter, 2007), cartopy (Met Office, 2010), and obspy (Beyreuther et al., 2010). We provide the simulated PGV maps that we used for training the ROMs at the public GitHub repository for this paper (Rekoske et al., 2023). This repository provides a Jupyter notebook which demonstrates using the iPOD reduced-order modeling technique to create ROMs for predicting new PGV maps.

### Acknowledgments

We would like to thank the Editor Rachel Abercrombie and the Associate Editor for their comments that helped to significantly improve this manuscript. We also greatly appreciate a review from Jack Muir who helped us improve the quality of the forward simulations and clarify our methodology, as well as an anonymous reviewer whose feedback helped us improve our presentation of the ROM error analysis and clarify the benefits of our reduced-order model. This material is based upon work supported by the National Science Foundation Graduate Research Fellowship Program under Grant No. DGE-2038238. Any opinions, findings, and conclusions or recommendations expressed in this material are those of the author(s) and do not necessarily reflect the views of the National Science Foundation. We gratefully acknowledge the Gauss Centre for Supercomputing e.V. ([www.gauss-centre.eu](http://www.gauss-centre.eu)) for providing computing time on the GCS Supercomputer SuperMUC-NG at Leibniz Supercomputing Centre ([www.lrz.de](http://www.lrz.de)), in project pn49ha. We acknowledge additional support from the National Science Foundation (NSF Grant No. EAR-2121568), the National Aeronautics and Space Administration (80NSSC20K0495), from the European Union’s Horizon 2020 Research and Innovation Programme (TEAR ERC Starting, grant No. 852992), Horizon Europe (DT-GEO, grant No. 101058129, Geo-INQUIRE,

grant No.101058518, and ChEESE-2P, grant No. 101093038), and the Southern California Earthquake Center (SCEC award 22135).

## References

- Aagaard, B. T., Hall, J. F., & Heaton, T. H. (2001). Characterization of near-source ground motions with earthquake simulations. *Earthquake Spectra*, *17*(2), 177–207.
- Abrahamson, N. A., Silva, W. J., & Kamai, R. (2014). Summary of the ASK14 ground motion relation for active crustal regions. *Earthquake Spectra*, *30*(3), 1025–1055.
- Anderson, J. G., & Brune, J. N. (1999). Probabilistic seismic hazard analysis without the ergodic assumption. *Seismological Research Letters*, *70*(1), 19–28.
- Audouze, C., De Vuyst, F., & Nair, P. (2009). Reduced-order modeling of parameterized PDEs using time–space–parameter principal component analysis. *International journal for numerical methods in engineering*, *80*(8), 1025–1057.
- Bailey, M. D., Bandyopadhyay, S., & Nychka, D. (2022). Adapting conditional simulation using circulant embedding for irregularly spaced spatial data. *Stat*, *11*(1), e446.
- Baker, J. W., Luco, N., Abrahamson, N. A., Graves, R. W., Maechling, P. J., & Olsen, K. B. (2014). Engineering uses of physics-based ground motion simulations. In *Proceedings of the tenth us conference on earthquake engineering*.
- Baltay, A. S., & Hanks, T. C. (2014). Understanding the magnitude dependence of pga and pgv in nga-west 2 data. *Bulletin of the Seismological Society of America*, *104*(6), 2851–2865.
- Baltay, A. S., Hanks, T. C., & Abrahamson, N. A. (2017). Uncertainty, variability, and earthquake physics in ground-motion prediction equations. *Bulletin of the Seismological Society of America*, *107*(4), 1754–1772.
- Benner, P., Gugercin, S., & Willcox, K. (2015). A survey of projection-based model reduction methods for parametric dynamical systems. *SIAM review*, *57*(4), 483–531.
- Berkooz, G., Holmes, P., & Lumley, J. L. (1993). The proper orthogonal decomposition in the analysis of turbulent flows. *Annual review of fluid mechanics*, *25*(1), 539–575.
- Beyreuther, M., Barsch, R., Krischer, L., Megies, T., Behr, Y., & Wassermann, J. (2010). ObsPy: A Python toolbox for seismology. *Seismological Research Letters*, *81*(3), 530–533.
- Bommer, J. J., Douglas, J., Scherbaum, F., Cotton, F., Bungum, H., & Fah, D. (2010). On the selection of ground-motion prediction equations for seismic hazard analysis. *Seismological Research Letters*, *81*(5), 783–793.
- Boore, D. M. (1983). Stochastic simulation of high-frequency ground motions based on seismological models of the radiated spectra. *Bulletin of the Seismological Society of America*, *73*(6A), 1865–1894. doi: 10.1785/BSSA07306A1865
- Boore, D. M. (2010). Orientation-independent, nongeometric-mean measures of seismic intensity from two horizontal components of motion. *Bulletin of the Seis-*

- mological Society of America*, 100(4), 1830–1835. doi: 10.1785/0120090400
- Böse, M., Smith, D. E., Felizardo, C., Meier, M.-A., Heaton, T. H., & Clinton, J. F. (2018). FinDer v.2: Improved real-time ground-motion predictions for M2–M9 with seismic finite-source characterization. *Geophysical Journal International*, 212(1), 725–742. doi: 10.1093/gji/ggx430
- Bozorgnia, Y., Abrahamson, N. A., Ahdi, S. K., Ancheta, T. D., Atik, L. A., Archuleta, R. J., . . . SJ Chiou, B. (2021). NGA-Subduction research program. *Earthquake Spectra*, 38(2), 783–798.
- Bozorgnia, Y., Abrahamson, N. A., Atik, L. A., Ancheta, T. D., Atkinson, G. M., Baker, J. W., . . . Chiou, B. S.-J. (2014). NGA-West2 research project. *Earthquake Spectra*, 30(3), 973–987.
- Breiman, L. (2001). Random forests. *Machine learning*, 45(1), 5–32.
- Brown, H. M., Allen, R. M., Hellweg, M., Khainovski, O., Neuhauser, D., & Souf, A. (2011). Development of the elarms methodology for earthquake early warning: Realtime application in California and offline testing in Japan. *Soil Dynamics and Earthquake Engineering*, 31(2), 188–200.
- Brune, J. N. (1970). Tectonic stress and the spectra of seismic shear waves from earthquakes. *Journal of Geophysical Research*, 75(26), 4997–5009.
- Bui-Thanh, T., Damodaran, M., & Willcox, K. (2003). Proper orthogonal decomposition extensions for parametric applications in compressible aerodynamics. In *21st aiaa applied aerodynamics conference* (p. 4213).
- Chung, A. I., Henson, I., & Allen, R. M. (2019). Optimizing earthquake early warning performance: ElarmS-3. *Seismological Research Letters*, 90(2A), 727–743. doi: 10.1785/0220180192
- Cochran, E. S., Bunn, J., Minson, S. E., Baltay, A. S., Kilb, D. L., Kodera, Y., & Hoshiaba, M. (2019). Event detection performance of the PLUM earthquake early warning algorithm in southern California. *Bulletin of the Seismological Society of America*, 109(4), 1524–1541.
- Cui, Y., Poyraz, E., Olsen, K. B., Zhou, J., Withers, K., Callaghan, S., . . . others (2013). Physics-based seismic hazard analysis on petascale heterogeneous supercomputers. In *Sc’13: Proceedings of the international conference on high performance computing, networking, storage and analysis* (pp. 1–12).
- De Marchi, S., & Schaback, R. (2010). Stability of kernel-based interpolation.
- Druault, P., Guibert, P., & Alizon, F. (2005). Use of proper orthogonal decomposition for time interpolation from PIV data. *Experiments in Fluids*, 39(6), 1009–1023. doi: 10.1007/s00348-005-0035-3
- Dumbser, M., & Käser, M. (2006). An arbitrary high-order discontinuous Galerkin method for elastic waves on unstructured meshes – II. The three-dimensional isotropic case. *Geophysical Journal International*, 167(1), 319–336. doi: 10.1111/j.1365-246X.2006.03120.x
- Engler, D. T., Worden, C. B., Thompson, E. M., & Jaiswal, K. S. (2022). Partitioning ground motion uncertainty when conditioned on station data. *Bulletin of the Seismological Society of America*, 112(2), 1060–1079.
- Field, E. H., Arrowsmith, R. J., Biasi, G. P., Bird, P., Dawson, T. E., Felzer, K. R.,

- ... others (2014). Uniform california earthquake rupture forecast, version 3 (ucerf3)—the time-independent model. *Bulletin of the Seismological Society of America*, *104*(3), 1122–1180.
- Frankel, A., Wirth, E., Marafi, N., Vidale, J., & Stephenson, W. (2018). Broadband synthetic seismograms for magnitude 9 earthquakes on the Cascadia megathrust based on 3D simulations and stochastic synthetics, part 1: Methodology and overall results. *Bulletin of the Seismological Society of America*, *108*(5A), 2347–2369.
- Frankel, A. D., Carver, D. L., & Williams, R. A. (2002). Nonlinear and linear site response and basin effects in seattle for the m 6.8 nisqually, washington, earthquake. *Bulletin of the Seismological Society of America*, *92*(6), 2090–2109.
- Furumura, T., Maeda, T., & Oba, A. (2019). Early forecast of long-period ground motions via data assimilation of observed ground motions and wave propagation simulations. *Geophysical Research Letters*, *46*(1), 138–147.
- Gallovič, F., Valentová, Ľ., Ampuero, J.-P., & Gabriel, A.-A. (2019). Bayesian dynamic finite-fault inversion: 1. method and synthetic test. *Journal of Geophysical Research: Solid Earth*, *124*(7), 6949–6969. doi: 10.1029/2019JB017510
- Geuzaine, C., & Remacle, J.-F. (2009). Gmsh: A 3-D finite element mesh generator with built-in pre-and post-processing facilities. *International journal for numerical methods in engineering*, *79*(11), 1309–1331.
- Goulet, C. A., Bozorgnia, Y., Kuehn, N., Al Atik, L., Youngs, R. R., Graves, R. W., & Atkinson, G. M. (2021). NGA-East ground-motion characterization model part I: Summary of products and model development. *Earthquake Spectra*, *37*(1.suppl), 1231–1282. doi: 10.1177/87552930211018723
- Graves, R., Jordan, T. H., Callaghan, S., Deelman, E., Field, E., Juve, G., ... Vahi, K. (2011). CyberShake: A physics-based seismic hazard model for Southern California. *Pure and Applied Geophysics*, *168*(3), 367–381. doi: 10.1007/s00024-010-0161-6
- Graves, R., & Pitarka, A. (2016). Kinematic ground-motion simulations on rough faults including effects of 3D stochastic velocity perturbations. *Bulletin of the Seismological Society of America*, *106*(5), 2136–2153.
- Guo, M., & Hesthaven, J. S. (2018). Reduced order modeling for nonlinear structural analysis using Gaussian process regression. *Computer methods in applied mechanics and engineering*, *341*, 807–826.
- Halton, J. H. (1960). On the efficiency of certain quasi-random sequences of points in evaluating multi-dimensional integrals. *Numerische Mathematik*, *2*(1), 84–90.
- Hartzell, S., Cranswick, E., Frankel, A., Carver, D., & Meremonte, M. (1997). Variability of site response in the los angeles urban area. *Bulletin of the Seismological Society of America*, *87*(6), 1377–1400.
- Hashash, Y. M., & Park, D. (2002). Viscous damping formulation and high frequency motion propagation in non-linear site response analysis. *Soil Dynamics and Earthquake Engineering*, *22*(7), 611–624.
- Heinecke, A., Breuer, A., Rettenberger, S., Bader, M., Gabriel, A.-A., Pelties, C., ...

- others (2014). Petascale high order dynamic rupture earthquake simulations on heterogeneous supercomputers. In *Sc'14: Proceedings of the international conference for high performance computing, networking, storage and analysis* (pp. 3–14).
- Hesthaven, J. S., Pagliantini, C., & Rozza, G. (2022). Reduced basis methods for time-dependent problems. *Acta Numerica*, *31*, 265–345.
- Hesthaven, J. S., & Ubbiali, S. (2018). Non-intrusive reduced order modeling of nonlinear problems using neural networks. *Journal of Computational Physics*, *363*, 55–78. doi: 10.1016/j.jcp.2018.02.037
- Hinton, G. E. (1990). Connectionist learning procedures. In *Machine learning* (pp. 555–610). Elsevier.
- Homma, T., & Saltelli, A. (1996). Importance measures in global sensitivity analysis of nonlinear models. *Reliability Engineering & System Safety*, *52*(1), 1–17.
- Hoshihara, M., & Aoki, S. (2015). Numerical shake prediction for earthquake early warning: Data assimilation, real-time shake mapping, and simulation of wave propagation. *Bulletin of the Seismological Society of America*, *105*(3), 1324–1338.
- Hough, S. E., Friberg, P., Busby, R., Field, E., Jacob, K., & Borchardt, R. (1990). Sediment-induced amplification and the collapse of the Nimitz Freeway. *Nature*, *344*(6269), 853–855.
- Hu, Z., Olsen, K. B., & Day, S. M. (2022). 0–5 Hz deterministic 3-D ground motion simulations for the 2014 La Habra, California, Earthquake. *Geophysical Journal International*, *230*(3), 2162–2182.
- Hunter, J. D. (2007). Matplotlib: A 2D graphics environment. *Computing in science & engineering*, *9*(03), 90–95.
- Julian, B. R., Miller, A. D., & Foulger, G. (1998). Non-double-couple earthquakes 1. theory. *Reviews of Geophysics*, *36*(4), 525–549.
- Käser, M., Hermann, V., & Puente, J. d. l. (2008). Quantitative accuracy analysis of the discontinuous galerkin method for seismic wave propagation. *Geophysical Journal International*, *173*(3), 990–999.
- Kingma, D. P., & Ba, J. (2017). *Adam: A Method for Stochastic Optimization* (No. arXiv:1412.6980). arXiv.
- Kodera, Y., Yamada, Y., Hirano, K., Tamaribuchi, K., Adachi, S., Hayashimoto, N., . . . Hoshihara, M. (2018). The propagation of local undamped motion (PLUM) method: A simple and robust seismic wavefield estimation approach for earthquake early warning. *Bulletin of the Seismological Society of America*, *108*(2), 983–1003.
- Kohler, M. D., Cochran, E. S., Given, D., Guiwits, S., Neuhauser, D., Henson, I., . . . Schwarz, S. (2017). Earthquake early warning ShakeAlert system: West coast wide production prototype. *Seismological Research Letters*, *89*(1), 99–107. doi: 10.1785/0220170140
- Komatitsch, D., & Tromp, J. (1999). Introduction to the spectral element method for three-dimensional seismic wave propagation. *Geophysical journal international*, *139*(3), 806–822.

- Krenz, L., Uphoff, C., Ulrich, T., Gabriel, A.-A., Abrahams, L., Dunham, E., & Bader, M. (2021). 3D acoustic-elastic coupling with gravity: the dynamics of the 2018 Palu, Sulawesi earthquake and tsunami. In *Proceedings of the international conference for high performance computing, networking, storage and analysis*. New York, NY, USA: ACM. doi: <https://doi.org/10.1145/3458817.3476173>
- Lazzaro, D., & Montefusco, L. B. (2002). Radial basis functions for the multivariate interpolation of large scattered data sets. *Journal of Computational and Applied Mathematics*, *140*(1-2), 521–536.
- Lye, K. O., Mishra, S., Ray, D., & Chandrashekar, P. (2021). Iterative surrogate model optimization (ismo): an active learning algorithm for pde constrained optimization with deep neural networks. *Computer Methods in Applied Mechanics and Engineering*, *374*, 113575.
- Meletti, C., Marzocchi, W., D’amico, V., Lanzano, G., Luzi, L., Martinelli, F., ... Visini, F. (2021). The new Italian seismic hazard model (MPS19). *Annals of Geophysics*, *64*(1).
- Met Office, U. K. (2010). Cartopy: A cartographic python library with a matplotlib interface. *Exeter, Devon*.
- Milner, K. R., Shaw, B. E., Goulet, C. A., Richards-Dinger, K. B., Callaghan, S., Jordan, T. H., ... Field, E. H. (2021). Toward physics-based nonergodic PSHA: A prototype fully deterministic seismic hazard model for southern California. *Bulletin of the Seismological Society of America*, *111*(2), 898–915.
- Moschetti, M. P., Hartzell, S., Ramírez-Guzmán, L., Frankel, A. D., Angster, S. J., & Stephenson, W. J. (2017). 3D ground-motion simulations of Mw 7 earthquakes on the Salt Lake City segment of the Wasatch fault zone: Variability of long-period ( $T \geq 1$  s) ground motions and sensitivity to kinematic rupture parameters. *Bulletin of the Seismological Society of America*, *107*(4), 1704–1723.
- Moseley, B., Markham, A., & Nissen-Meyer, T. (2018). Fast approximate simulation of seismic waves with deep learning. *arXiv preprint arXiv:1807.06873*.
- Moseley, B., Nissen-Meyer, T., & Markham, A. (2020). Deep learning for fast simulation of seismic waves in complex media. *Solid Earth*, *11*(4), 1527–1549. doi: [10.5194/se-11-1527-2020](https://doi.org/10.5194/se-11-1527-2020)
- Nagata, T., Nakai, K., Yamada, K., Saito, Y., Nonomura, T., Kano, M., ... Nagao, H. (2023). Seismic wavefield reconstruction based on compressed sensing using data-driven reduced-order model. *Geophysical Journal International*, *233*(1), 33–50.
- Oba, A., Furumura, T., & Maeda, T. (2020). Data assimilation-based early forecasting of long-period ground motions for large earthquakes along the Nankai trough. *Journal of Geophysical Research: Solid Earth*, *125*(6), e2019JB019047.
- Olsen, K., Day, S., & Bradley, C. (2003). Estimation of  $q$  for long-period ( $\geq 2$  sec) waves in the los angeles basin. *Bulletin of the Seismological Society of America*, *93*(2), 627–638.
- Olsen, K. B., Day, S. M., Minster, J. B., Cui, Y., Chourasia, A., Faerman, M., ...

- Jordan, T. (2006). Strong shaking in Los Angeles expected from southern San Andreas earthquake. *Geophysical Research Letters*, *33*(7). doi: 10.1029/2005GL025472
- Pagani, S., & Manzoni, A. (2021). Enabling forward uncertainty quantification and sensitivity analysis in cardiac electrophysiology by reduced order modeling and machine learning. *International Journal for Numerical Methods in Biomedical Engineering*, *37*(6), e3450.
- Parker, G. A., & Baltay, A. S. (2022). Empirical map-based nonergodic models of site response in the Greater Los Angeles area. *Bulletin of the Seismological Society of America*, *112*(3), 1607–1629.
- Pearson, K. (1895). Vii. note on regression and inheritance in the case of two parents. *proceedings of the royal society of London*, *58*(347-352), 240–242.
- Pedregosa, F., Varoquaux, G., Gramfort, A., Michel, V., Thirion, B., Grisel, O., ... Duchesnay, É. (2011). Scikit-learn: Machine Learning in Python. *Journal of Machine Learning Research*, *12*(85), 2825–2830.
- Petersen, M. D., Shumway, A. M., Powers, P. M., Mueller, C. S., Moschetti, M. P., Frankel, A. D., ... Boyd, O. S. (2020). The 2018 update of the US National Seismic Hazard Model: Overview of model and implications. *Earthquake Spectra*, *36*(1), 5–41.
- Pitarka, A., Akinci, A., De Gori, P., & Buttinelli, M. (2022). Deterministic 3D Ground-Motion Simulations (0–5 Hz) and Surface Topography Effects of the 30 October 2016 M w 6.5 Norcia, Italy, Earthquake. *Bulletin of the Seismological Society of America*, *112*(1), 262–286.
- Rasht-Behesht, M., Huber, C., Shukla, K., & Karniadakis, G. E. (2022). Physics-informed neural networks (PINNs) for wave propagation and full wave-form inversions. *Journal of Geophysical Research: Solid Earth*, *127*(5), e2021JB023120.
- Rekoske, J., Gabriel, A. A., & May, D. (2023). *jrekoske/Instantaneous-PhysicsBased-GroundMotionMaps: Publication release (Version 1.0.0)* [Software]. Zenodo. Retrieved from <https://doi.org/10.5281/zenodo.8170242> doi: 10.5281/zenodo.8170242
- Rettenberger, S., Meister, O., Bader, M., & Gabriel, A.-A. (2016). Asagi: A parallel server for adaptive geoinformation. In *Proceedings of the exascale applications and software conference 2016* (p. 2:1-2:9). New York, NY, USA: ACM. doi: <https://doi.org/10.1145/2938615.2938618>
- Ripperger, J., Mai, P. M., & Ampuero, J.-P. (2008). Variability of near-field ground motion from dynamic earthquake rupture simulations. *Bulletin of the Seismological Society of America*, *98*(3), 1207–1228.
- Rodgers, A. J., Pitarka, A., Pankajakshan, R., Sjögreen, B., & Petersson, N. A. (2020, August). Regional-Scale 3D Ground-Motion Simulations of Mw 7 Earthquakes on the Hayward Fault, Northern California Resolving Frequencies 0–10 Hz and Including Site-Response Corrections. *Bulletin of the Seismological Society of America*, *110*(6), 2862–2881. doi: 10.1785/0120200147
- Sahakian, V. J., Baltay, A., Hanks, T. C., Buehler, J., Vernon, F. L., Kilb, D., &

- Abrahamson, N. A. (2019). Ground motion residuals, path effects, and crustal properties: A pilot study in Southern California. *Journal of Geophysical Research: Solid Earth*, *124*(6), 5738–5753. doi: 10.1029/2018JB016796
- Savran, W., & Olsen, K. (2020). Kinematic rupture generator based on 3-d spontaneous rupture simulations along geometrically rough faults. *Journal of Geophysical Research: Solid Earth*, *125*(10), e2020JB019464.
- SCEDC. (2013). *Southern California Earthquake Data Center*. Retrieved from <https://scedc.caltech.edu> doi: <https://doi.org/10.7909/C3WD3xH1>
- Shaw, J. H., Plesch, A., Tape, C., Suess, M. P., Jordan, T. H., Ely, G., . . . Munster, J. (2015). Unified structural representation of the Southern California crust and upper mantle. *Earth and Planetary Science Letters*, *415*, 1–15. doi: 10.1016/j.epsl.2015.01.016
- Small, P., Gill, D., Maechling, P. J., Taborda, R., Callaghan, S., Jordan, T. H., . . . Goulet, C. (2017). The SCEC unified community velocity model software framework. *Seismological Research Letters*, *88*(6), 1539–1552.
- Smith, J. D., Azizzadenesheli, K., & Ross, Z. E. (2020). Eikonet: Solving the eikonal equation with deep neural networks. *IEEE Transactions on Geoscience and Remote Sensing*, *59*(12), 10685–10696.
- Spudich, P., Rowshandel, B., Shahi, S. K., Baker, J. W., & Chiou, B. S.-J. (2014). Comparison of NGA-West2 directivity models. *Earthquake Spectra*, *30*(3), 1199–1221.
- Stirling, M., McVerry, G., Gerstenberger, M., Litchfield, N., Van Dissen, R., Berryman, K., . . . Jacobs, K. (2012). National Seismic Hazard Model for New Zealand: 2010 Update. *Bulletin of the Seismological Society of America*, *102*(4), 1514–1542. doi: 10.1785/0120110170
- Stone, I., Wirth, E. A., & Frankel, A. D. (2022). Topographic response to simulated Mw 6.5–7.0 earthquakes on the Seattle Fault. *Bulletin of the Seismological Society of America*, *112*(3), 1436–1462.
- Swischuk, R., Mainini, L., Peherstorfer, B., & Willcox, K. (2019). Projection-based model reduction: Formulations for physics-based machine learning. *Computers & Fluids*, *179*, 704–717. doi: 10.1016/j.compfluid.2018.07.021
- Taborda, R., & Bielak, J. (2013). Ground-motion simulation and validation of the 2008 Chino Hills, California, earthquake. *Bulletin of the Seismological Society of America*, *103*(1), 131–156.
- Tamhidi, A., Kuehn, N., Ghahari, S. F., Rodgers, A. J., Kohler, M. D., Taciroglu, E., & Bozorgnia, Y. (2021, September). Conditioned Simulation of Ground-Motion Time Series at Uninstrumented Sites Using Gaussian Process Regression. *Bulletin of the Seismological Society of America*, *112*(1), 331–347. doi: 10.1785/0120210054
- Taufiqurrahman, T., Gabriel, A.-A., Ulrich, T., Valentová, L., & Gallovič, F. (2022). Broadband Dynamic Rupture Modeling With Fractal Fault Roughness, Frictional Heterogeneity, Viscoelasticity and Topography: The 2016 Mw 6.2 Amatrice, Italy Earthquake. *Geophysical Research Letters*, *49*(22), e2022GL098872. doi: 10.1029/2022GL098872

- Thompson, M., Hartog, J. R., & Wirth, E. A. (2022). Effect of Fixing Earthquake Depth in ShakeAlert Algorithms on Performance for Intraslab Earthquakes. *Seismological Research Letters*, *93*(1), 277–287. doi: 10.1785/0220210056
- Thompson, M., Wirth, E. A., Frankel, A. D., Renate Hartog, J., & Vidale, J. E. (2020). Basin amplification effects in the Puget Lowland, Washington, from strong-motion recordings and 3D simulations. *Bulletin of the Seismological Society of America*, *110*(2), 534–555. doi: 10.1785/0120190211
- Tromp, J., Komatitsch, D., Hjørleifsdóttir, V., Liu, Q., Zhu, H., Peter, D., . . . Hutko, A. (2010). Near real-time simulations of global CMT earthquakes. *Geophysical Journal International*, *183*(1), 381–389. doi: 10.1111/j.1365-246X.2010.04734.x
- Trugman, D. T., & Shearer, P. M. (2018). Strong correlation between stress drop and peak ground acceleration for recent M 1–4 earthquakes in the San Francisco Bay Area. *Bulletin of the Seismological Society of America*, *108*(2), 929–945. doi: 10.1785/0120170245
- Uphoff, C., Rettenberger, S., Bader, M., Madden, E., Ulrich, T., Wollherr, S., & Gabriel, A.-A. (2017b). Extreme scale multi-physics simulations of the tsunamigenic 2004 Sumatra megathrust earthquake. In *Proceedings of the international conference for high performance computing, networking, storage and analysis, sc 2017*. doi: <https://doi.org/10.1145/3126908.3126948>
- Uphoff, C., Rettenberger, S., Bader, M., Madden, E. H., Ulrich, T., Wollherr, S., & Gabriel, A.-A. (2017a). Extreme scale multi-physics simulations of the tsunamigenic 2004 sumatra megathrust earthquake. In *Proceedings of the international conference for high performance computing, networking, storage and analysis* (pp. 1–16).
- van Driel, M., Krischer, L., Stähler, S. C., Hosseini, K., & Nissen-Meyer, T. (2015). Instaseis: Instant global seismograms based on a broadband waveform database. *Solid Earth*, *6*(2), 701–717.
- Virtanen, P., Gommers, R., Oliphant, T. E., Haberland, M., Reddy, T., Cournapeau, D., . . . Bright, J. (2020). SciPy 1.0: Fundamental algorithms for scientific computing in Python. *Nature methods*, *17*(3), 261–272.
- Wald, D. J., Lin, K.-W., & Quitoriano, V. (2008). *Quantifying and qualifying USGS ShakeMap uncertainty*. US Geological Survey Reston, VA.
- Wald, D. J., Quitoriano, V., Worden, C. B., Hopper, M., & Dewey, J. W. (2011). USGS “Did You Feel It?” Internet-based macroseismic intensity maps. *Annals of Geophysics*, *54*(6). doi: 10.4401/ag-5354
- Wang, X., & Zhan, Z. (2020). Moving from 1-D to 3-D velocity model: Automated waveform-based earthquake moment tensor inversion in the Los Angeles region. *Geophysical Journal International*, *220*(1), 218–234.
- Willcox, K., & Peraire, J. (2002). Balanced model reduction via the proper orthogonal decomposition. *AIAA journal*, *40*(11), 2323–2330.
- Withers, K. B., Moschetti, M. P., & Thompson, E. M. (2020). A machine learning approach to developing ground motion models from simulated ground motions. *Geophysical Research Letters*, *47*(6), e2019GL086690.

- Withers, K. B., Olsen, K. B., Shi, Z., & Day, S. M. (2018). Validation of deterministic broadband ground motion and variability from dynamic rupture simulations of buried thrust earthquakes. *Bulletin of the Seismological Society of America*, *109*(1), 212–228. doi: 10.1785/0120180005
- Worden, C. B., Thompson, E. M., Baker, J. W., Bradley, B. A., Luco, N., & Wald, D. J. (2018). Spatial and spectral interpolation of ground-motion intensity measure observations. *Bulletin of the Seismological Society of America*, *108*(2), 866–875. doi: 10.1785/0120170201
- Worden, C. B., & Wald, D. J. (2016). *ShakeMap 4 Manual — ShakeMap Documentation documentation*. <http://usgs.github.io/shakemap/>.
- Xiao, D., Fang, F., Pain, C., & Hu, G. (2015). Non-intrusive reduced-order modelling of the Navier–Stokes equations based on RBF interpolation. *International Journal for Numerical Methods in Fluids*, *79*(11), 580–595.
- Yang, Y., Gao, A. F., Azizzadenesheli, K., Clayton, R. W., & Ross, Z. E. (2023). Rapid seismic waveform modeling and inversion with neural operators. *IEEE Transactions on Geoscience and Remote Sensing*.
- Yang, Y., Gao, A. F., Castellanos, J. C., Ross, Z. E., Azizzadenesheli, K., & Clayton, R. W. (2021). Seismic wave propagation and inversion with neural operators. *The Seismic Record*, *1*(3), 126–134.